Setting the cornerstone for a family of models for gravitational waves from compact binaries: The dominant harmonic for nonprecessing quasicircular black holes

Geraint Pratten,[1,2,*] Sascha Husa,[2] Cecilio García-Quirós,[2] Marta Colleoni,[2] Antoni Ramos-Buades,[2] Héctor Estellés,[2] and Rafel Jaume[2]

[1]*School of Physics and Astronomy and Institute for Gravitational Wave Astronomy, University of Birmingham, Edgbaston, Birmingham B15 9TT, United Kingdom*

[2]*Departament de Física, Universitat de les Illes Balears, IAC3—IEEC, Carretera de Valldemossa km 7.5, E-07122 Palma, Spain*

(Received 19 February 2020; accepted 29 July 2020; published 2 September 2020)

In this paper we present IMRPHENOMXAS, a thorough overhaul of the IMRPHENOMD [S. Husa *et al.*, Phys. Rev. D **93**, 044006 (2016); S. Khan *et al.*, Phys. Rev. D **93**, 044007 (2016)] waveform model, which describes the dominant $l = 2$, $|m| = 2$ spherical harmonic mode of nonprecessing coalescing black holes in terms of piecewise closed form expressions in the frequency domain. Improvements include in particular the accurate treatment of unequal spin effects, and the inclusion of extreme mass ratio waveforms. IMRPHENOMD has previously been extended to approximately include spin precession [M. Hannam *et al.*, Phys. Rev. Lett. **113**, 151101 (2014)] and subdominant spherical harmonics [L. London *et al.*, Phys. Rev. Lett. **120**, 161102 (2018)], and with its extensions it has become a standard tool in gravitational wave parameter estimation. Improved extensions of IMRPHENOMXAS are discussed in companion papers [C. García-Quirós *et al.*, Phys. Rev. D **102**, 064002 (2020); G. Pratten *et al.*, arXiv:2004.06503].

DOI: 10.1103/PhysRevD.102.064001

I. INTRODUCTION

A key element of gravitational wave data analysis are waveform models, which serve as templates that detector data can be compared with, usually in the context of matched filter techniques, combined with template-bank based searches [1,2], or Bayesian inference [3,4]. For general relativity, significant effort has been spent by the gravitational wave source modeling community to construct such models as approximate solutions of the Einstein equations, combining perturbative methods, numerical solutions, and qualitative insight. The science case of gravitational wave astronomy is limited by the fidelity of the models to the complex physical processes they represent, and the computational efficiency of evaluating the models. For GW150914 [5,6], the first detection and loudest binary black hole event of the first two observation runs [7], a detailed investigation of the effects of systematic errors in the waveform models was carried out in [8] for the models used for the analysis of the event: the time domain "SEOBNR" family of models based on the effective one-body approach [9–13], and the phenomenological frequency domain model IMRPHENOMP [14]. The latter extends the IMRPHENOMD model [15,16] for the dominant, i.e., $l = 2$, $|m| = 2$, spherical harmonic modes of quasicircular black hole binaries to include effects of spin-precession. No evidence was found "for a systematic bias relative to the statistical error of the original parameter recovery of GW150914 due to modeling approximations or modeling inaccuracies," however more accurate models would be required for future observations.

In this paper we present IMRPHENOMXAS, a thorough update to the IMRPHENOMD model [15,16]. Following the phenomenological modeling framework, IMRPHENOMXAS is formulated in the frequency domain, and describes the waveform in terms of piecewise closed form expressions, with the aim to facilitate computationally efficient applications in gravitational wave data analysis. In a companion paper we present an extension to subdominant harmonics, which is aimed to supersede IMRPHENOMHM [17], which is only been calibrated to numerical relativity data for the dominant quadrupole spherical harmonic. In a second companion paper [18] we present a method to accelerate the evaluation of the waveform model, based on earlier work by Vinciguerra *et al.* [19]. In future work we will discuss extending our model to precession [20] using the methods of IMRPHENOMP [14,21].

The main elements of the model construction are chosen as follows: The waveform is split into two real non-oscillatory functions, an amplitude and phase. Modeling then proceeds in two steps: first, closed form expressions are fitted to numerical waveform data for a set of calibration waveforms. These calibration waveforms are constructed as

*g.pratten@bham.ac.uk

hybrid waveforms, appropriately gluing together approximate waveforms describing the inspiral, which in our case we take as the SEOBNRv4 version of an effective-one-body (EOB) model [12], and numerical relativity waveforms, which describe the last orbits, merger, and ringdown of the system. Finding appropriate analytical functions becomes easier as the frequency region for the fitting procedure is broken up into smaller regions. As with previous phenomenological waveform models, we choose three such regions, where the ansatz in each one and the choice of transition frequencies are guided by perturbative descriptions and physical intuition: (i) A low frequency inspiral regime, where the waveform can be described by adding additional terms to a post-Newtonian expansion. (ii) A high frequency regime where the waveform is dominated by quasinormal ringdown. (iii) An intermediate regime, which captures the complex physics of the merger and the transition between the physics of the inspiral and the ringdown, where neither the post-Newtonian nor the quasinormal-ringdown perturbative descriptions apply.

The result of the first step is a set of coefficients for each numerical waveform, which greatly compress the information used to accurately represent each waveform. In a second step, each coefficient is then modeled across the three-dimensional parameter space of nonprecessing quasicircular black hole binaries, described by mass ratio and the two spin components orthogonal to the orbital plane. In contrast to previous frequency domain phenomenological models, IMRPHENOMXAS captures the full spin dependence of the waveform: In the models preceding IMRPHENOMD [22,23], a single effective spin was used to model the spin-dependence. In IMRPHENOMD, different effective spins were used to model the inspiral and high-frequency regime, which already significantly reduced the parameter bias for unequal spin cases [24]. In IMRPHENOMXAS, we use the hierarchical fitting method developed in [25] to finally treat the full three-dimensional parameter space.

IMRPHENOMXAS also significantly increases the validity range in the mass ratio of any previous phenomenological model by including extreme mass ratio waveforms up to mass ratio 1000, which were computed by hybridizing numerical solutions of the perturbative Teukolsky equation [26–28] as described in [29]. Due to improvements in the model construction and the larger number of input calibration waveforms, IMRPHENOMXAS offers a significant improvement in accuracy, showing ∼1–2 orders of magnitude improvement in the mismatch compared to IMRPHENOMD. For a list of the key features implemented in IMRPHENOMXAS see Sec. X.

The paper is organized as follows: First we provide a detailed discussion of our conventions in Sec. II. Then we present our input waveforms in Sec. III. The mapping between phenomenological coefficients and physical parameters is discussed in Sec. IV, and the choice of transition frequencies between the model's three frequency regions is treated in Sec. V. The model construction for the amplitude and phase is then described in Secs. VI and VII, and an example of our use of the hierachical fitting procedure for parameter space fits is provided in Sec. VIII. In Sec. IX we describe how we have validated our model, and we conclude with a summary and discussion of our work in Sec. X. Appendix A provides the details of the post-Newtonian TaylorF2 approximant as we use it.

II. CONVENTIONS AND PRELIMINARIES

A. Intrinsic parameters conventions

We consider binary systems of astrophysical black holes in general relativity, which do not exhibit spin precession and are quasicircular (noneccentric). In the limit of large separation, each black hole is perfectly described by the Kerr solution, and the initial conditions for the dynamics are given by the position and velocity vectors (or equivalently momenta) of the two black holes. In this limit the momenta correspond to Newtonian particles in a circular orbit, and we will adopt the center-of-mass frame. The intrinsic parameters $\boldsymbol{\theta}$ of such systems correspond to the dimensionless projections of the BH spins (intrinsic angular momenta) $\vec{S}_{1,2}$ in the preserved direction of the orbital angular momentum $\vec{L}$, and the masses $m_{1,2}$, where

$$\chi_i = \frac{\vec{S}_i \cdot \vec{L}}{m_i^2 |\vec{L}|}. \tag{2.1}$$

We define the mass ratio $q = m_1/m_2 \geq 1$, total mass $M = m_1 + m_2$, and symmetric mass ratio $\eta = m_1 m_2/M^2$.

B. Waveform conventions

IMRPHENOMXAS models the $\ell = |m| = 2$ spherical harmonic modes of the coalescence of binary systems of nonprecessing quasicircular black holes. We assume a sense of rotation of the binary consistent with a right-handed coordinate system: The orbital frequency vector $\vec{\omega}$ is chosen in the direction of the z-axis of a Cartesian coordinate system (x, y, z). The black holes orbit in the plane $z = 0$, and the spacetime, and thus the gravitational-wave signal, exhibits equatorial symmetry, i.e., the northern hemisphere $z \geq 0$ is isometric to the southern hemisphere $z \leq 0$.

We introduce a standard spherical coordinate system

$$x = r\cos\varphi\cos\vartheta, \quad y = r\sin\varphi\cos\vartheta, \quad z = r\cos\vartheta, \tag{2.2}$$

and spherical harmonics $Y^{-2}_{\ell m}$ of spin-weight -2 (see, e.g., [30]), where here we will only require the modes:

$$Y^{-2}_{2\pm2} = \sqrt{\frac{5}{64\pi}}(1 \pm \cos\vartheta)^2 e^{\pm 2i\varphi}. \tag{2.3}$$

The gravitational-wave strain h depends on an inertial time coordinate t, the angles ϑ, φ in the sky of the source, and the source parameters $\boldsymbol{\theta}$. It is written in terms of spherical harmonic modes $h_{\ell m}$, and alternatively in terms of gravitational wave polarizations h_+ and $h_\times$ as

$$h(t,\vartheta,\varphi;\boldsymbol{\theta}) = \sum_{m=-2,2} h_{2m}(t;\boldsymbol{\theta})\,{}_{-2}Y_{2m}(\vartheta,\varphi), \tag{2.4}$$

$$= h_+(t,\vartheta,\varphi;\boldsymbol{\theta}) - i h_\times(t,\vartheta,\varphi;\boldsymbol{\theta}). \tag{2.5}$$

We define the Fourier transform to be consistent with the conventions adopted in the LIGO Algorithms Library [31]

$$\tilde{h}(f) = \int_{-\infty}^{\infty} h(t) e^{-i2\pi f t} dt. \tag{2.6}$$

With this convention of the Fourier transform time derivatives are converted to multiplications by factors of $i2\pi f$ in the Fourier domain. The frequency domain strain $\tilde{h}$ can then be written in the form of the time domain strain in (2.4), (2.5),

$$\tilde{h}(f,\vartheta,\varphi;\boldsymbol{\theta}) = \sum_{m=-2,2} \tilde{h}_{2m}(f;\boldsymbol{\theta})\,{}_{-2}Y_{2m}(\vartheta,\varphi) \tag{2.7}$$

$$= \tilde{h}_+(f,\vartheta,\varphi;\boldsymbol{\theta}) - i\tilde{h}_\times(f,\vartheta,\varphi;\boldsymbol{\theta}). \tag{2.8}$$

The equatorial symmetry of nonprecessing binaries implies

$$h_{22}(t) = h^*_{2-2}(t), \tag{2.9}$$

it is thus sufficient to model just one spherical harmonic. For the Fourier transform this leads to

$$\tilde{h}_{22}(f) = \tilde{h}^*_{2-2}(-f). \tag{2.10}$$

Our above choices imply that if the time domain modes are written in terms of a positive amplitude $a_{\rm TD}(t)$ and a phase $\phi_{\rm TD}(t)$, then

$$h_{22}(t) = a_{\rm TD}(t) e^{-i\phi_{\rm TD}(t)}, \quad h_{2-2}(t) = a_{\rm TD}(t) e^{i\phi_{\rm TD}(t)}. \tag{2.11}$$

Since we assume negligible eccentricity the frequency time derivative of the phases of both modes are monotonic functions of t. We will assume right-handed circular motion for the binary, with the rotation axis being the z-axis defined by (2.2). With the definitions (2.11), (2.3) this implies that $\phi_{\rm TD}(t)$ is then a monotonically *increasing* function of time and the gravitational-wave polarizations in the time domain are given by

$$h_+(t) = +\sqrt{\frac{5}{4\pi}}\frac{1+\cos^2\vartheta}{2}\cdot a_{\rm TD}\cos(2\varphi - \phi_{\rm TD}), \tag{2.12}$$

$$h_\times(t) = -\sqrt{\frac{5}{4\pi}}\cos\vartheta\cdot a_{\rm TD}\sin(2\varphi - \phi_{\rm TD}). \tag{2.13}$$

With our convention for the Fourier transformation (2.6), the definitions above imply that $\tilde{h}_{22}(f)$ is concentrated in the negative frequency domain and $\tilde{h}_{2-2}(f)$ in the positive frequency domain. For the inspiral, this can be checked against the stationary phase approximation (SPA), see, e.g., [32–34] or the derivation in Appendix B.

We construct our model in the frequency domain, it is thus convenient to model the $\tilde{h}_{2-2}$, which is nonzero for positive frequencies. The mode $\tilde{h}_{22}$, defined for negative frequencies, can then be computed from (2.10). We model the Fourier amplitude $A(f>0,\boldsymbol{\theta})$, which is a positive function for positive frequencies, and zero otherwise, and the Fourier domain phase $\phi(f>0,\boldsymbol{\theta})$, defined by

$$\tilde{h}_{2-2}(f,\boldsymbol{\theta}) = A(f,\boldsymbol{\theta}) e^{-i\phi(f,\boldsymbol{\theta})}. \tag{2.14}$$

The gravitational wave polarizations in the frequency domain are then given by

$$\tilde{h}_+(f) = +\sqrt{\frac{5}{16\pi}}\frac{1+\cos^2\vartheta}{2}\cdot \tilde{h}_{2-2} e^{-i2\varphi}, \tag{2.15}$$

$$\tilde{h}_\times(f) = -i\sqrt{\frac{5}{16\pi}}\cos\vartheta\cdot \tilde{h}_{2-2} e^{-i2\varphi}. \tag{2.16}$$

When one only carries out computations with the projections of the gravitational strain onto detectors, i.e., specific polarizations, one only deals with Fourier transforms of real functions, and only positive frequencies are required.

Note that with the above definitions, for a face-on binary, i.e., $\vartheta = 0$, we get that $\tilde{h} = \tilde{h}_+ - i\tilde{h}_\times = 0$. This does not mean that the signal vanishes for face-off binaries, but that when working with the full waveform without projection onto specific polarizations, one would also need to explicitly consider negative frequencies.

As a consequence of time derivatives being related to multiplication in Fourier space, the conversion between the GW strain and the Newman-Penrose scalar ψ_4, where

$$\frac{d^2 h(t)}{dt^2} = \psi_4(t), \tag{2.17}$$

is given by

$$\tilde{h}(f) = -\frac{\tilde{\psi}_4(f)}{4\pi^2 f^2}, \tag{2.18}$$

and only affects the Fourier domain amplitude, but not the phase, up to a jump of π, and apart from possible effects

specific to the numerical algorithm used to carry out this conversion.

A time shift of the waveform is encoded only in the Fourier domain phase, but at the price of changing the shape of phase function. The Fourier transformation of a time and phase shifted function $h_{\varphi_0,\tau} = h(t-\tau)e^{i\varphi_0}$ is given by

$$\begin{aligned}\tilde{h}_{\varphi_0,\tau}(\omega) &= \int_{-\infty}^{\infty} h(t-\tau)e^{i\varphi_0}e^{-i\omega t}dt \\ &= e^{i(\varphi_0+\omega\tau)}\int_{-\infty}^{\infty} h(t')e^{-i\omega t'}dt', \\ &= e^{i(\varphi_0+\omega\tau)}\tilde{h}, \end{aligned} \tag{2.19}$$

and thus corresponds to an additional term in the phase, which is linear in frequency.

An additional ambiguity arises due to the choice of tetrad defining the polarizations. This is discussed in detail in [29,35] and, for the dominant quadrupole mode, is equivalent to a fixed global rotation of the source.

C. Waveform phenomenology preliminaries

A detailed discussion of the phenomenology of the inspiral-merger-ringdown frequency domain waveforms modeled here has been given in [15]. Here we summarize some of the key features which are most relevant for our modeling strategy.

Our goal is to describe the amplitude and phase of the waveform by piecewise closed form expressions, which are valid in some frequency interval. Using more such intervals makes the modeling of each interval simpler: e.g., when using a sufficient number of intervals a cubic spline representation may be sufficient. Using a smaller number of intervals makes it harder to find an appropriate analytical form for each interval.

In this work, we will use three regimes: For the inspiral, i.e., for low frequencies, it is natural to describe the waveform in the framework of post-Newtonian theory (see, e.g., [36]) as a Taylor expansion in powers of v/c, where v is an orbital velocity parameter and c the speed of light, or equivalently a frequency f, where $\pi f = (v/c)^3$. One can then simply add higher order terms in v/c, often referred to as pseudo-post-Newtonian terms, where as-of-yet unknown coefficients are calibrated to the data set of numerical waveforms. More concretely, we will base our inspiral description on the standard TaylorF2 approximant [37–40], which provides closed form expressions for the amplitude and phase of the Fourier transform of the gravitational wave strain for quasicircular inspirals, and is derived from time domain post-Newtonian expressions via the stationary phase approximation, see Appendixes A and B. We augment the known TaylorF2 series with higher order terms as described in Sec. VI A for the amplitude, and in Sec. VII A for the phase.

After the merger, the relaxation of the excited final black hole to the Kerr solution can be described by black hole perturbation theory and quasinormal ringdown behavior [41]. While the stationary phase approximation is not valid for the merger and ringdown, it has long been known that simple models of damped oscillations can be Fourier-transformed analytically, and thus can serve to analytically model key features of the ringdown in the frequency domain. We will briefly discuss such models below, and how they can be used to form the basis of the closed-form frequency domain model we want to construct.

We use a third, intermediate, frequency regime to capture the transition between the inspiral and ringdown regimes. This transition regime roughly corresponds to the merger, and models the complex physics that occurs when the spacetime is highly dynamical and so far eludes a perturbative treatment. A crucial element of modeling this intermediate regime is to find an appropriate start frequency, when the inspiral breaks down, in the sense that an inconveniently large number of post-Newtonian orders would be required for an accurate description. For extreme mass ratios, the innermost circular orbit gives a good estimate of this frequency, but it is not appropriate for comparable masses, where we have found the minimal energy circular orbit (MECO) as defined by [42] provides a good estimate.

We now return to the description of the ringdown in the frequency domain, and will discuss simple analytical models to motivate how we proceed. For the simple damped oscillation

$$h(t) = \Theta(t)e^{2\pi(if_{\rm RD}t - f_{\rm damp}|t|)}, \tag{2.20}$$

where $\Theta(t)$ denotes the Heaviside theta function, the Fourier transform is

$$\tilde{h}(f) = \frac{1}{2\pi(f_{\rm damp} + i(f-f_{\rm RD}))}, \tag{2.21}$$

with absolute value

$$|\tilde{h}(f)| = \frac{1}{2\pi\sqrt{f_{\rm damp}^2 + (f-f_{\rm RD})^2}}, \tag{2.22}$$

and phase derivative

$$\frac{d\arg\tilde{h}(f)}{df} = -\frac{1}{2\pi}\frac{f_{\rm damp}}{f_{\rm damp}^2 + (f-f_{\rm RD})^2}. \tag{2.23}$$

The quasinormal mode frequencies are thus imprinted on the Fourier domain amplitude and phase derivative through a Lorentzian function for the phase derivative, and its square root for the amplitude, with a falloff of $1/f$ for high frequencies. The physical waveform should however fall

off faster than any polynomial due to its smoothness, since for smooth functions $h(t)$ one has that (see, e.g., [43])

$$\tilde{h}(f) = O(|f|^{-|M|}) \quad \text{as} \quad |f| \to \infty \quad \text{for all } M. \tag{2.24}$$

If a function $h(t)$ only has $p-1$ continuous derivatives in L^2 for some $p \geq 0$ and a pth derivative in L^2 of bounded variation,[1] then [43] (see also the discussion in [15]):

$$\tilde{h}(f) = O(|f|^{-p-1}) \quad \text{as} \quad |f| \to \infty. \tag{2.25}$$

Other variants of the example of Eq. (2.20) are, e.g., replacing t by $|t|$ and dropping the theta function, or replacing the complex exponential by a sine or cosine (see, e.g., [44,45]), which leads to minor modifications in the results, such as a faster polynomial falloff of the amplitude.

This has motivated to model the frequency domain ringdown amplitude as a Lorentzian for the early phenomenological waveform models [22,23,46,47]. For the IMRPHENOMD model the Lorentzian amplitude ansatz has been modified with a decaying exponential to be consistent with the falloff expected from smooth functions, and the falloff rate has been calibrated to numerical relativity waveforms. A rough estimate of the falloff rate can be obtained with a smooth ansatz for the time domain waveform. Inspecting the Newman-Penrose quantity ψ_4 around the merger for numerical relativity waveforms, one finds that it is roughly symmetric around the peak. This symmetry has also been found in a recent approximate analytical calculation [48]. Following [48] for the amplitude ansatz for ψ_4, but making the unrealistic assumption that the gravitational wave frequency is constant around the amplitude peak, we get that for

$$\psi_4(t) = \frac{e^{2\pi t(if_{\rm RD} - f_{\rm damp})}}{e^{2\pi t f_{\rm damp}} + e^{-2\pi t f_{\rm damp}}} \tag{2.26}$$

the Fourier transform is

$$\tilde{\psi}_4(f) = \frac{1}{2\pi(f_{\rm damp} + i(f - f_{\rm RD}))}, \tag{2.27}$$

For large frequencies the amplitude falls off as

$$\tilde{\psi}_4(f) \sim e^{-\pi(f - f_{\rm RD})/(2f_{\rm damp})}. \tag{2.28}$$

We have compared the asymptotic falloff rate of $-\pi/(2f_{\rm damp})$ with our hybrid data set, and find that it typically overestimates the numerical data, but only by a factor within 1.32–1.38 for 90% of the cases, which is surprisingly good giving the crudeness of the model (2.26). For the ringdown amplitude, we will thus essentially follow the IMRPHENOMD ansatz of a Lorentzian, multiplied with an exponential damping factor.

For the phase derivative in the high frequency regime, modifications of the simple model leads to Lorentzians with added background terms, in the form

$$\frac{d\phi}{df} = \frac{a}{(f - f_{\rm RD})^2 + (2f_{\rm damp})^2} + \text{background}, \tag{2.29}$$

which are consistent with our numerical data. For IMRPHENOMD the ringdown regime was thus modeled as a Lorentzian, plus a polynomial in f^{-1}. We will follow the same strategy with two main modifications: First we will modify how to represent the polynomial that models the "background" term. Second, we note that $f_{\rm damp}$ has a very large dynamic range. For negative spins, $f_{\rm damp}$ is quite large and leads to very broad Lorentzians, which are not confined to the ringdown region. An overview of frequencies that play a crucial role in designing our modeling approach is shown in Fig. 1. As the figure shows, all the frequencies exhibit significant variation, which requires a corresponding dynamic range in the transition frequencies between the three frequency regions of the model.

The loss of accuracy and gradual breakdown of the post-Newtonian series expansion for high frequencies as the merger is approached also determines the frequency regime where numerical solutions are required to provide unambiguous approximate solutions and error estimates. The

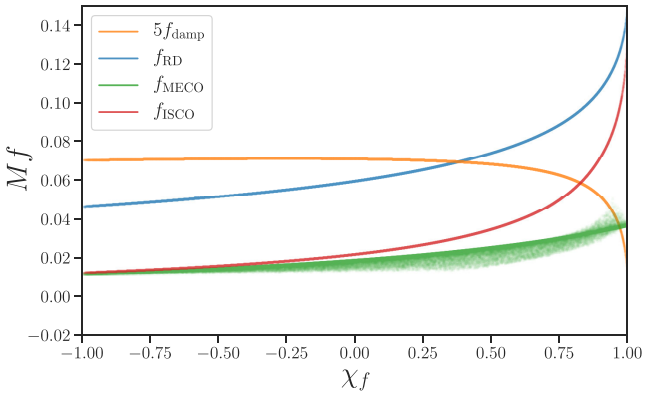

FIG. 1. The ringdown $f_{\rm RD}$, damping $f_{\rm damp}$, ISCO $f_{\rm ISCO}$ and $f_{\rm MECO}$ frequencies are plotted for a random sample of binaries from the nonprecessing parameter space as functions of the dimensionless Kerr parameter χ_f of the remnant black hole calculated using NR calibrated fits to the final state [25]. A negative sign of χ_f corresponds to binaries for which the orbital angular momentum points in the opposite direction to the spin of the (final) black hole. The maximum of $f_{\rm MECO}$ occurs for equal black holes with maximal component spins aligned with the orbital angular momentum, and the minimum for the extreme mass ratio limit with maximal antialigned component spins.

[1]The L^2-norm of a function $u(x)$ is defined by $\|u\| = [\int_{-\infty}^{\infty} |u(x)|^2 dx]^{1/2}$. The symbol L^2 denotes the set of functions for which this integral is finite: $L^2 = \{u : \|u\| < \infty\}$.

computational cost of such simulations increases drastically as the initial frequency is lowered, the leading order post-Newtonian estimate for the time to merger T for start frequency f_0 is

$$T \propto \frac{f_0^{-8/3}}{\eta}. \tag{2.30}$$

Covering densely the parameter space that we want to model with numerical relativity waveforms with start frequencies lower than the sensitive band of our detectors is still prohibitively expensive, and we will thus use "hybrid" waveforms as our input data set, where numerical relativity waveforms are appropriately glued to an inspiral description derived from the post-Newtonian expansion, as discussed below in Sec. III.

III. INPUT WAVEFORMS

The primary input data we use for developing, calibrating, and evaluating the IMRPHENOMXAS waveform model is the set of hybrid waveforms described in [29]. These waveforms are constructed by appropriately gluing together numerical waveforms, which cover the last orbits, merger and ringdown, with an inspiral model. For comparable masses up to mass ratio 18, the numerical waveforms have been computed by solving the full Einstein field equations using the methods of numerical relativity. The inspiral model is taken to be an EOB resummation of post-Newtonian waveforms. For extreme mass ratios we use numerical solutions for linearized gravitational waves in a Kerr background, sourced by EOB dynamics, as described below.

The EOB approach provides a framework to extend the validity of post-Newtonian results [49,50] with resummation techniques, and to incorporate additional information, such as a calibration to numerical relativity results, which has lead to families of time-domain models for the complete waveform, from inspiral to ringdown [10,12,51]. Here we use the recent SEOBNRv4 [12] EOB model to hybridize with numerical relativity waveforms. For IMRPHENOMD, the SEOBNRv2 approximant [10] was used, removing however the calibrations to numerical relativity in order to decrease the dependence between the two models. Here we use the original calibrated SEOBNRv4 model, as our goal is to maximize the accuracy of the resulting waveform model.

SEOBNRv4 has in fact been calibrated to numerical waveforms, and describes the complete waveform from inspiral to ringdown. We could thus also augment our calibration data set with SEOBNRv4 waveforms in regions of the parameter space where numerical relativity waveforms are sparse. In the model presented here, we only use such SEOBNRv4 waveforms at low frequencies in the inspiral, i.e., well below the MECO frequency, where very little to no NR information is present. For the intermediate and merger-ringdown regions, only EOB-NR hybrids and test-particle hybrids are used to calibrate the waveform model.

The comparable mass numerical relativity waveforms used in the hybrid data set have been produced with SPEC [52–58]), which uses pseudospectral numerical methods and black-hole excision, as well as with the BAM [59,60] and EINSTEIN TOOLKIT [61] codes.

The BAM code solves the $3+1$ decomposed Einstein field equations using the χ-variant [62] of the moving-punctures implementation of the BSSN formulation [63–65]. Spatial derivatives are computed using sixth-order accurate finite differencing stencils [60]. Kreiss-Oliger dissipation terms converge at fifth order, and a fourth-order Runge-Kutta algorithm is used for the time evolution. BBH puncture initial data [66,67] are calculated with a pseudo-spectral elliptic solver described in Ref [68]. The GWs are calculated using the Newman-Penrose scalar ψ_4 and extracted at a finite distance from the source.

The EINSTEIN TOOLKIT simulations use Bowen-York initial data [66,67] computed using the `TwoPunctures` thorn [68]. Time evolution is performed using the W-variant [69] of the BSSN formulation of the Einstein field equations as implemented by MCLACHLAN [70]. The BHs are evolved using standard moving punctures gauge-conditions [62,71]. The lapse is evolved according to the $1+\log$ condition [72] and the shift according to the hyperbolic $\tilde{\Gamma}$-driver [73]. Simulations are performed using 8th order accurate finite difference stencils with Kreiss-Oliger dissipation [74]. Adaptive mesh refinement is provided by CARPET [75,76], with the wave-extraction zone being computed on spherical grids using the LLAMA multi-patch infrastructure [77]. Low eccentricity initial data is produced following the procedure outlined in [78]. Further details will be given in [29].

SPEC is a multidomain pseudospectral code [53,54,79] that uses excision to remove the BH interiors, thereby removing the BH singularity from the computational domain. The code evolves the generalized harmonic coordinate formulation of the Einstein field equations [79–82] with constraint damping. Initial data is constructed using the extended conformal thin sandwich (XCTS) equations [83–85], with newer simulations typically choosing the conformal metric and trace of the extrinsic curvature to be a weighted superposition of two single BHs in Kerr-Schild coordinates [86]. Boundary conditions imposed on the excision boundaries ensure that these boundaries are apparent horizons [53–55,79]. Further details can be found in [87].

We used 186 waveforms from the public SXS catalog as of 2018 [57]. After the release of the latest SXS collaboration catalog, [87], we extended the dataset to incorporate 355 SPEC simulations and updated the parameter space fits for the phase accordingly. We opted not to update the amplitude fits to incorporate the latest SpEC simulations as

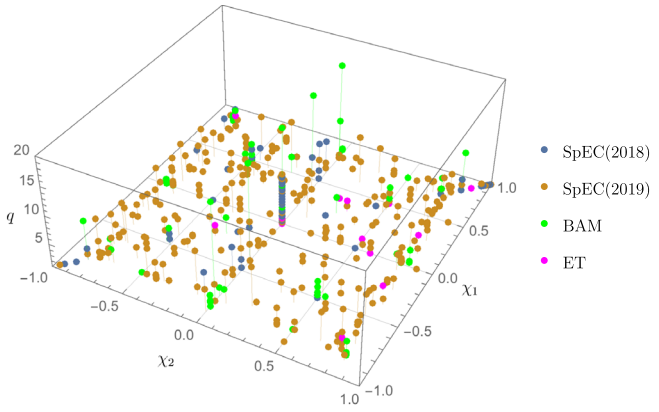

FIG. 2. The mass ratio and spins for the NR waveforms used in the calibration of IMRPHENOMXAS. SXS simulations are shown in blue [57] and orange [87], BAM simulations in green and EINSTEIN TOOLKIT simulations in pink.

this is anticipated to have a smaller impact on the overall accuracy of the waveform model.

The 95 BAM waveforms consists of previously published and new waveforms. The EINSTEIN TOOLKIT simulations have been recently produced by the authors. For further details on the BAM and EINSTEIN TOOLKIT waveforms see [29].

The key data sets that determine the calibration range of our waveform model are the BAM waveforms for a range of spins at mass ratio 1:18, high-spin BAM and SXS waveforms at mass ratios 4 and 8, and equal mass SXS data sets at very high spins of -0.95 and $+0.994$.

The coverage of the comparable mass parameter space is shown in Fig. 2.

As the computational cost of NR simulations diverges rapidly as $\eta \to 0$, no systematic NR simulations are available for mass ratios $q \geq 18$. This severely limits the parameter space against which we can calibrate a waveform model to NR. Constraining the asymptotic behavior of the parameter space fits in the extreme-mass-ratio limit is essential for well-behaved extrapolation and to reduce uncertainty in the waveform model for intermediate-mass-ratio binaries, where NR coverage is extremely sparse. For many of the coefficients appearing in our waveform model, no fully analytical knowledge, with complete spin dependence, is available and we instead opt to constrain the fits by calibrating against semianalytical waveforms in the test-particle limit.

As in [88], the simulations for BBH mergers in the test-particle limit are produced using TEUKODE [26–28], which combines a semi-analytical description of the dynamics with a time-domain numerical approach for computing the full multipolar waveform. The dynamics of the binary are prescribed using EOB dynamics, where conservative geodesic motion has been augmented with a linear-in-η radiation reaction [89,90]. This makes use of the factorized and resummed circularized waveform introduced in [9,91] and uses PN information up to 5.5PN. The fluxes are computed by solving the Regge-Wheeler-Zerilli (RWZ) $1+1$ equations (nonspinning) or the Teukolsky $2+1$ equations (spinning). These equations are solved in the time domain using a hyperboloidal foliation and horizon-penetrating coordinates that allow for the unambiguous extraction of radiation at $\mathcal{I}^+$ (future null infinity) [26,92,93].

As with the NR simulations detailed above, the test-particle waveforms are hybridized against a longer EOB inspiral. For the calibration of IMRPHENOMXAS, we use two sets of waveforms: one set at $q = 200$ and the other set at $q = 1000$. The spin of the primary BH spans an interval $[-0.9, 0.9]$ and the secondary BH is taken to be nonspinning.

The waveforms in the test-particle limit should only be treated as approximate as $\mathcal{O}(\eta)$ effects are neglected in the conservative dynamics and the 5PN-accurate EOB-resummed analytical multipolar waveforms, used to build the radiation reaction force, show relatively poor performance. A more detailed discussion on some of the observed discrepancies between the comparable-mass limit and the extreme-mass-ratio limit will be given below.

A recently proposed framework for the factorization and resummation of the residual waveform amplitudes [94–96] is expected to improve the self-consistency of the test-particle waveforms and hence the self-consistency of the calibration. A discussion of different approaches to resummation and the radiation reaction in the context of effective one body models can be found in [97,98]. A detailed study of the consistency of IMRPHENOMXAS in the test-particle limit will be presented elsewhere.

IV. MAPPING PHENOMENOLOGICAL COEFFICIENTS TO PHYSICAL PARAMETERS

The model here has 8 amplitude coefficients and 13 phase coefficients, meaning that there are 21 phenomenological coefficients that must be mapped to the physical 3D parameter space $(\eta, \hat{S}, \delta\chi)$, where $\hat{S}$ is an effective spin parametrization of our choice and $\delta\chi = \chi_1 - \chi_2$ is the linear-in-spin difference. The mapping procedure detailed here is a generalization of the approach taken in previous phenomenological models and pioneered in fits to the radiated energy, final mass and final spin [25,88]. Here we use a hierarchical, bottom-up approach to calibrate fits to numerical relativity waveforms. As in previous post-Newtonian studies, the dominant parameter dependencies are on the mass ratio and effective spin parametrizations. The remaining unequal spin contribution is subdominant and can be effectively modeled by working to linear order in the spin difference. We provide a representative example of this workflow in Sec. VIII and a flowchart of the logic behind the hierarchical fitting procedure is shown in Fig. 3.

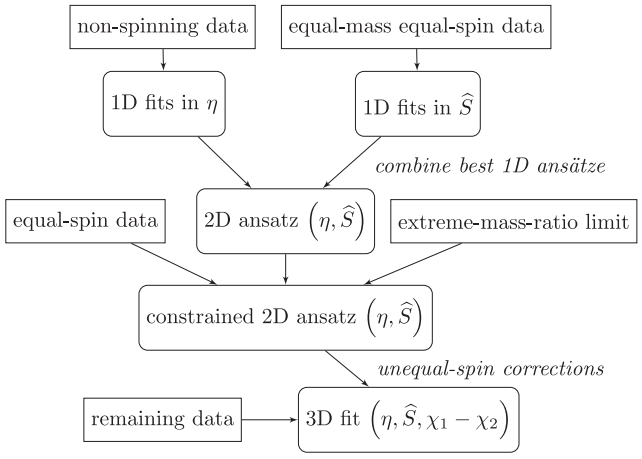

FIG. 3. Flowchart for the hierarchical parameter space fits, taken from Fig. 1 of [25]. The starting point are one-dimensional submanifolds, taken to be the equal mass and spin limit and the nonspinning limit. The next step is to use a given spin parametrization $\hat{S}$ to perform an expansion about the 1D fits. Finally, the residuals between the data and the 2D fits are used to fit for unequal spin contributions.

A. Collocation points

Direct calibration of the phenomenological coefficients to the hybrid data can often be problematic due to poor numerical conditioning. This is notable during inspiral, where both poor convergence and the eventual breakdown of the PN series can lead to numerical instabilities for the pseudo-PN coefficients used to capture higher frequency behavior. Such coefficients typically alternate in sign leading to significant numerical cancellations that must be captured accurately across the parameter space.

The previous calibration of a phenomenological waveform models typically reduced to fitting a polynomial of order n, $P_n(x)$, to the input EOB-NR hybrid data $f(x)$ and producing a fit for the coefficients of the polynomial across the binary parameter space (η, χ_1, χ_2). However, due to the considerations above, we instead adopt a slightly different strategy and opt to reconstruct a phenomenological model by solving a linear system of equations that requires us to know the value of the amplitude or phase derivative at a set of fixed frequency nodes or *collocation points*. In this section, we outline the choice of these collocation points and how it allows us to both optimally sample the hybrid data and optimally reconstruct a phenomenological model.

The Weierstraß approximation theorem [99] states that for any continuous real valued function on an interval $[a, b]$ and $\epsilon > 0$, there exists a polynomial $P_n(x)$ such that for all $x \in [a, b]$ we have $|f(x) - p(x)| < \epsilon$. However, a well known caveat to this theorem is that the result is highly dependent on the set of polynomials used and on their convergence. In particular, use of equidistant nodes when constructing $P_n(x)$ can lead to oscillatory divergences from $f(x)$ as we increase the degree of the polynomial. This is known as Runge's phenomena and results in unphysical oscillations that can impact the accuracy of the model. In order to help alleviate such issues, there are a number of possible options. For instance, we could help tame oscillatory behavior by fitting to a lower degree polynomial or we could construct multiple overlapping subintervals constructed with low-degree polynomials, i.e., piecewise polynomial interpolation. Instead, the strategy adopted here, and in [100], is to choose the interpolation nodes $\{x^i\}_{i=0}^n$ such that the maximum error $\|e_n(x)\|_\infty$ is minimized, where the error is $e_n(x) = f(x) - P_n(x)$ and $\|\cdot\|_\infty$ denotes the $L-\infty$ norm.[2] This can be achieved by selecting $(n+1)$ sample points for the polynomial $P_n(x)$ at the roots of the Chebyshev polynomial. For nodes on an arbitrary interval $[a, b]$, this reduces to

$$x_k = \frac{1}{2}(a+b) + \frac{1}{2}(b-a)\cos\left[\frac{(2k-1)\pi}{2n}\right], \tag{4.1}$$

where $k = 1, \ldots, n$. There are a few key advantages to using Chebyshev nodes when constructing such phenomenological fits. First, the error will be the smallest for all polynomials of degree n. Second, the error can often be more uniformly distributed over the interval in which we perform the fit. Finally, the error decreases exponentially with n, leading to spectral convergence of the fit

$$\|e_n\| \leq \frac{\|f^{(n+1)}\|_\infty}{2^n(n+1)!}. \tag{4.2}$$

In contrast, the error from using equidistant nodes scales approximately as $\|e_n\| \leq \|f^{(n+1)}\|_\infty h^{n+1}/4(n+1)$, where h is the spacing between the nodes. For these reasons, we find it optimal to use collocation points evaluated at the Chebyshev nodes in the domain of interest.

The next step is to fit the value of the amplitude or phase derivative evaluated at these collocation points across the binary parameter space (η, χ_1, χ_2) using the hierarchical procedure discussed in the next section. Using the values of the amplitude or phase derivative at the collocation points, or their differences, we can reconstruct the underlying phenomenological model by solving a system of linear equations using standard methods, such as an LU factorization

$$F(f_i) = v_i, \tag{4.3}$$

where $F = \varphi'(f)$ or $A(f)$, f_i are the collocation points, i.e., the frequencies at the Gauss-Chebyshev nodes, and v_i are the values of the hybrid evaluated at the collocation points.

[2]The $L-\infty$ or max-norm is defined by $\|f\|_\infty \equiv \|f\|_{L_\infty[a,b]} = \max_{t\in[a,b]}|f(t)|$.

B. Hierarchical fitting procedure: One-dimensional subspace fits

As was just discussed, in order to evaluate a phenomenological waveform model, we must be able to reconstruct the phenomenological coefficients given the intrinsic parameters (η, χ_1, χ_2) of the binary. To solve the linear system of equations that allows us reconstruct the phenomenological ansatz, we require a fit across the parameter space for the values of the amplitude and phase derivative evaluated at the collocation points. In this section, we detail the hierarchical procedure used to construct the fits dimension-by-dimension.

The hierarchical fits are performed dimension-by-dimension, focusing first on the simplest and best-sampled subspaces in the EOB-NR hybrid data set, the nonspinning and equal-mass equal-spin waveforms. The spin parametrization $\hat{S}$ used to construct the fit is a free choice and will differ from region to region. The various parametrizations employed in this paper are discussed in Sec. IV E.

The fits are constructed using *Mathematica*'s `NonlinearModelFit` function, where we use both polynomial and rational ansätze, as in [25,88]. Fits using rational functions can often fail to converge due to the existence of singularities in the rational functions themselves. In order to alleviate issues related to nonconvergence, we use high-dimensional polynomials to construct a Padé approximant to a given order, whose coefficients are then used to precondition the starting values for the rational function fits [25,88]. Rational functions with a numerator of polynomial order m and a denominator of polynomial order k will be denoted as an ansatz of order (m, k). The use of rational functions offers numerous advantages to high-dimensional polynomials. In particular we find that rational functions are smoother, less prone to unphysical oscillations and extrapolate in a more controlled manner.

We obtain $F(\eta; \hat{S} = 0)$ fits for a large set of polynomial and rational functions. In order to avoid overfitting the data, we rank the fits using their goodness of fit and the Bayesian information criteria, allowing us to penalize fits that carry redundant coefficients. The general functional form of the nonspinning fits can be written as

$$F(\eta; \hat{S} = 0) = \frac{\sum_i a_i \eta^i}{1 + \sum a_j \eta^j}. \tag{4.4}$$

The general form of the 2D ansatz will be given as the sum of nonspinning and spinning contributions. We will therefore need to constrain the constant term of the 1D ansatz in $\hat{S}$ in order to reproduce the equal-mass, nonspinning result, i.e., $F(\eta = 0.25; \hat{S} = 0)$ must be identical for both 1D fits. The general form of the equal-mass, equal-spin fits is therefore written as

$$F(\eta = 0.25, \hat{S}) = \frac{\sum_i b_i \hat{S}^i}{1 + \sum_j b_j \hat{S}^j} + F(\eta = 0.25; \hat{S} = 0), \tag{4.5}$$

where the constant term is equivalent to Eq. (4.4) in the limit $\eta \to 0.25$. As above, the fits are ranked according to the goodness of fit and the Bayesian information criterion.

C. Hierarchical fitting procedure: Two-dimensional subspace fits

The next step in the hierarchical framework is to construct the two-dimensional fits spanning the $(\eta, \hat{S})$ subspace. The ansatz from the 1D fit in Eq. (4.5) is reexpanded with a polynomial of order J in order to capture 2D curvature associated to $\hat{S}$-dependent terms via

$$b_i \to b_i \sum_{j=0}^{j=J} f_{ij} \eta^j, \tag{4.6}$$

where b_i are the coefficients of the 1D equal-mass, equal-spin fit. The general 2D ansatz for a phenomenological coefficient is therefore

$$F(\eta, \hat{S}) = F(\eta, 0) - F(0.25, 0) + F(0.25, \hat{S}, f_{ij}). \tag{4.7}$$

The order to which we expand in η is dependent upon the behavior of the phenomenological coefficient that is being fitted. Typically we find that expanding to third order in η $(J = 3)$ is the lowest order that leaves sufficient freedom to incorporate the constraints from the 1D fits and the extreme mass ratio limit as well as to adequately capture all the features of the data set. At higher order in η, numerous pathologies outside the calibration regime can start to develop, leading to a significant degradation in the performance of the calibrated model. In order to avoid potential singularities, appropriate care must be taken to remove pathological coefficients from the denominator of the rational ansatz.

D. Hierarchical fitting procedure: Unequal spin contributions and 3D fits

The final stage in the hierarchical approach is to incorporate the subdominant effect of unequal spins. Here we parametrize this effect by $\Delta\chi = \chi_1 - \chi_2$. The residuals are defined by subtracting the 2D equal spin fit from the fit against the unequal-spin NR cases:

$$\Delta F(\eta, \hat{S}, \Delta\chi) = F(\eta, \hat{S}, \Delta\chi) - F(\eta, \hat{S}). \tag{4.8}$$

This procedure can be done at discrete points in the symmetric mass ratio provided that sufficient unequal spin NR simulations are available.

At a given mass ratio, the residuals form a 2D surface $(\hat{S}, \Delta\chi, \Delta\lambda)$ which can be used to informatively construct an ansatz for the unequal spin effects. As with many aspects of phenomenological waveform modeling, insight can be taken from studying the structure of the post-Newtonian equations. For example, if we consider the next-to-leading order (NLO) spin-orbit (SO) contribution to the flux

$$\mathcal{F}^{\rm NLO}_{\rm SO} \propto \left(-\frac{9}{2}+\frac{272}{9}\eta\right)+\sqrt{1-4\eta}\left(-\frac{13}{16}+\frac{43}{4}\eta\right)\Sigma_\ell, \tag{4.9}$$

where

$$\Sigma_\ell = (m_2\chi_{2\ell} - m_1\chi_{1\ell}). \tag{4.10}$$

By inspection, the linear-in-spin difference contribution is killed by a factor of $\delta = \sqrt{1-4\eta}$ in the equal mass limit. Away from equal masses, the unequal spin contribution is a simple polynomial function in η. By comparison, the leading-order (LO) spin-spin (SS) term is given by

$$\mathcal{F}^{\rm LO}_{\rm SS} \propto x^2\left(8S_\ell^2 + 8\delta\Sigma_\ell S_\ell + \left(\frac{33}{16}-8\eta\right)\Sigma_\ell^2\right), \tag{4.11}$$

where

$$S_\ell = m_1^2\chi_{1\ell} + m_2^2\chi_{2\ell}. \tag{4.12}$$

In the equal mass limit the mixed term $\Sigma_\ell S_\ell$ is killed by a factor of δ but we still have a nonvanishing quadratic-in-spin-difference term Σ_ℓ^2.

In practice, we find that the 2D surfaces are typically close to flat, suggesting that the unequal spin effects are dominated by a linear dependence on $\Delta\chi$ and a possible mixture term $\hat{S}\Delta\chi$. This linear dependence will break down in the equal mass limit as, under an exchange of χ_1 and χ_2, terms linear in $\Delta\chi$ will vanish. In this limit, the surface is approximately parabolic and well-modeled by a quadratic term.

Based on the above considerations, we use a general ansatz with three spin-difference terms

$$\Delta F(\eta, \hat{S}, \Delta\chi) = A_1(\eta)\Delta\chi + A_2(\eta)\Delta\chi^2 + A_3(\eta)\Delta\chi\hat{S}. \tag{4.13}$$

The resulting full 3D ansatz is therefore given by

$$F(\eta, \hat{S}, \Delta\chi) = F(\eta, \hat{S}) + \Delta F(\eta, \hat{S}, \Delta\chi). \tag{4.14}$$

Additional higher order terms in the effective spin or spin difference are not used as there is no motivation from either PN or visual inspection of the residuals. In addition, the intrinsic error of the NR simulations begins to dominate and caution is required to ensure that we do not overfit noisy data. As a check, we follow the approach in [25] and perform four fits in $\Delta\chi$ for the values of A_i: linear, linear + quadratic, linear + mixed and the sum of all three contributions. Broadly, we find little evidence for quadratic and mixed contributions, with the linear spin-difference term dominating the fits.

E. Choice of spin parametrization

A choice that must be made when constructing the fits across the parameter space is the spin parametrization, $\hat{S}$, employed. The choice of parametrization can help minimize errors when building fits on a subspace of the data. One of the most widely used spin parametrizations is the effective aligned spin [22,37,101]

$$\chi_{\rm eff} = \frac{m_1\chi_1 + m_2\chi_2}{M}. \tag{4.15}$$

This choice was made in early Phenomenological waveform models IMRPHENOMB [22] and IMRPHENOMC [23]. In IMRPHENOMD, an alternative spin parametrization was used based on the reduced spin parameter, that describes the leading order spin-orbit term at 1.5PN in the amplitude and the phase [102,103]

$$\chi_{\rm PN} = \chi_{\rm eff} - \frac{38\eta}{113}(\chi_1+\chi_2), \tag{4.16}$$

normalized to $[-1, 1]$ for any mass ratio

$$\hat{\chi}_{\rm PN} = \frac{\chi_{\rm PN}}{1-76\eta/113}. \tag{4.17}$$

This PN motivated parametrization is particularly suited to use in IMR waveform models [104] and was also found to best capture spin-orbit contributions to the binding energy [105]. We will adopt $\hat{\chi}_{\rm PN}$ as our spin parametrization of choice for the inspiral regime.

For the final state, however, the underlying physics is best captured by the linear spin combination $S_1 + S_2$. We therefore find it useful to employ an effective total spin parameter

$$\hat{S}_{\rm tot} = \frac{S}{m_1^2+m_2^2}, \quad \text{with} \quad S = m^2\chi_1 + m^2\chi_2, \tag{4.18}$$

which was found to work well for final-state quantities [15,25]. In IMRPHENOMXAS, we will use $\hat{S}_{\rm tot}$ to parametrize the fits to the intermediate and merger-ringdown coefficients. A detailed study of the impact of different spin parametrizations is beyond the scope of this paper.

V. MATCHING REGIONS

Following the strategy adopted in previous phenomenological waveform models [15,16,22,23,47], we split the

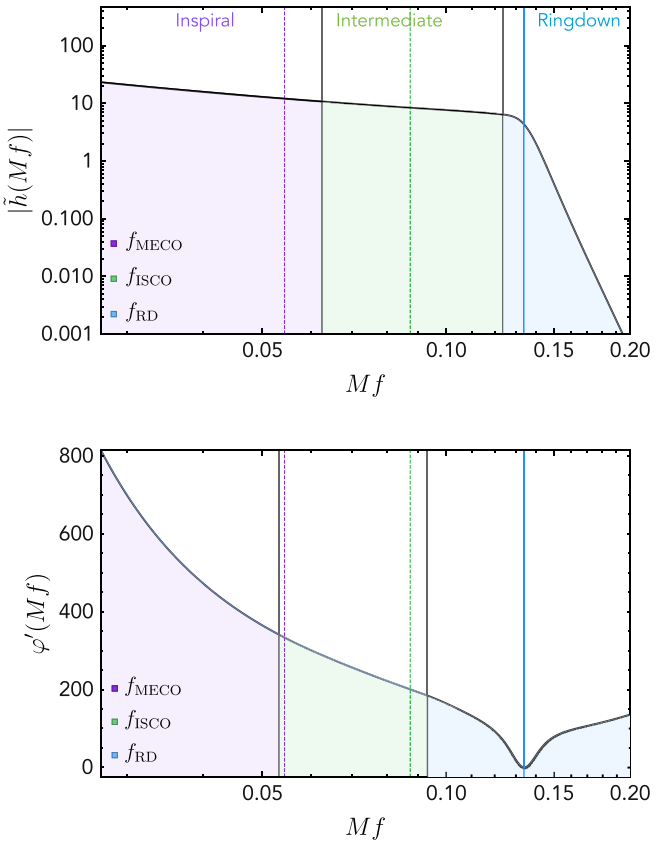

FIG. 4. Transition regions for the amplitude and phase derivative $\varphi' = \partial_f \varphi(f)$. The purple shaded area shows the *inspiral* region, green shaded the *intermediate* and the blue shaded the *merger ringdown*. The three colored lines show the MECO (purple), ISCO (green) and ringdown (blue) frequencies respectively.

waveform into three frequency regions and model each of these regimes separately. This is done for both the amplitude and the phase derivative. In this section we define these regions and explicitly highlight the calibration range used in determining the fits as well as the transition windows used when reconstructing the phenomenological model. These regions are highlighted in Fig. 4.

A. Inspiral

Two of the key improvements of IMRPHENOMXAS over IMRPHENOMD concern the frequency region over which the model is calibrated to the hybrid data. For IMRPHENOMD this region was

$$0.0035 \leq Mf \leq 0.018. \tag{5.1}$$

In IMRPHENOMXAS the lower frequency has been reduced to

$$Mf_0 = 0.0026 \tag{5.2}$$

which corresponds to lowering the starting frequency from 71.1 Hz to 52.8 Hz for a binary of total mass of 10 $M_\odot$, or to lowering the binary mass for which the calibration completely covers frequencies above 10 Hz from 71.1 $M_\odot$ to 52.8 $M_\odot$. We find that this change significantly improves matches between hybrids and the model for lower masses. The reason for not lowering the starting frequency further has been twofold: First, we build our hybrid waveforms in the time domain, and need to Fourier transform the hybrids on an equispaced frequency grid. In order to simplify our setup, we choose this frequency grid to be the same for all our waveforms. In order to achieve sufficient resolution at high frequencies, we choose a time step of $t/M = 0.5$. The start frequency is chosen to conveniently fit the complete hybrid generation in the time and frequency domain into the RAM available on a laptop for mass ratios up to about 500, as described in [29]. Allowing for windowing and robustly cutting away different types of artifacts restricts the low frequency limit that can be achieved. In future editions of the model, a more flexible approach will be used to further reduce the start frequency. The second reason is that a further reduction of start frequency would only be useful with further studies of how to best model the inspiral (e.g., regarding the order of pseudo-PN terms used, and the number of collocation points used). These studies are outside the scope of the present paper, but will be required for a more accurate representation of the extreme mass ratio limit, and possibly for further increases in accuracy.

In IMRPHENOMD, the maximal frequency for the inspiral description in terms of a modified post-Newtonian ansatz, was also fixed, irrespective of the binary's mass ratio or spin. In the extreme mass ratio case, an appropriate choice of transition frequency is given by the ISCO (innermost stable circular orbit) frequency, which can be evaluated in closed form, and ranges from $Mf \approx 0.006$ for inspiral into an extreme Kerr black hole with orbital angular momentum antialigned with the spin of the large black hole, to $Mf \approx 0.08$ for the aligned case. A fixed transition frequency from the inspiral to the intermediate regime is thus clearly not appropriate for extreme mass ratios, but also not for comparable masses where the dynamical range is smaller.

A natural termination frequency for the inspiral, which also applies to comparable masses, can be based on the minimum energy circular orbit (MECO) frequency. In a standard binary black hole inspiral, the orbital energy will gradually decrease until it reaches some minimum. The MECO is defined to be the orbit at which the orbital energy reaches its minimum value. Naturally, the MECO is implicitly tied to the PN order under consideration, which can be problematic in the extreme mass ratio limit where the PN approximation is poorly convergent. In order to alleviate such problems, [42] implemented a hybrid-MECO in which test-particle dynamics are folded into the PN approximation in order to provide a well-defined MECO condition valid for all spins. Schematically, the hybrid energy is constructed by replacing the test-particle limit of

the PN energy with the exact orbital energy per unit mass for a test-particle around a Kerr black hole [42]

$$E^{\rm Hybrid} = \frac{E^{n-\rm PN}}{\eta} - \left(\sum_{x=0}^{x=2n} E^{\rm Kerr}(v^x)\right) + E^{\rm Kerr} \tag{5.3}$$

where

$$E^{\rm Kerr} = \left(\frac{1-2w+\chi w^{3/2}}{\sqrt{1-3w+2\chi w^{3/2}}} - 1\right), \tag{5.4}$$

and $w = v^2/(1-\chi v^3)^{2/3}$. This expression was shown to have a minimum for currently known PN orders. In practice, we use a phenomenological fit to the hybrid-MECO as a natural PN approximation to the end of the inspiral. This alleviates the necessity of performing a root-finding operation when evaluating the waveform model.

The inspiral calibration range for the amplitude (A) and the phase (φ) is taken to be

$$f^{\varphi}_{C,\rm Ins} \in [0.0026, 1.02 f_{\rm MECO}], \tag{5.5}$$

$$f^{A}_{C,\rm Ins} \in [0.0026, 1.025 f^{A}_{T}], \tag{5.6}$$

where the C explicitly denotes the calibration domain and

$$f^{A}_{T} = f_{\rm MECO} + \frac{1}{4}(f_{\rm ISCO} - f_{\rm MECO}). \tag{5.7}$$

However, when building the waveform, the inspiral region interval is defined by

$$f^{\varphi}_{\rm Ins} \in (0, f_{\rm MECO} - \delta_R) \tag{5.8}$$

$$f^{A}_{\rm Ins} \in (0, f^{A}_{T}], \tag{5.9}$$

where

$$f^{\varphi}_{T} = 0.6\left(\frac{1}{2} f_{\rm RD} + f_{\rm ISCO}\right), \tag{5.10}$$

$$\delta_R = 0.03(f^{\varphi}_{T} - f_{\rm MECO}). \tag{5.11}$$

The inspiral region corresponds to the purple-shaded region in Fig. 4.

B. Intermediate regime

The intermediate regime is introduced in order to phenomenologically bridge the gap between the post-Newtonian regime and the perturbative black hole ringdown regime. The start of this region is determined by the breakdown of post-Newtonian theory and the end of the region is set relative to the ISCO and ringdown frequencies. This enables us to implicity incorporate a natural hierarchy of frequencies in a standard binary black hole inspiral: $f_{\rm MECO} < f_{\rm ISCO} < f_{\rm ring}$.

For the intermediate region, the calibration domain is taken to be

$$f^{\varphi}_{C,\rm Int} \in [f_{\rm MECO} - \delta_R, f^{\varphi}_{T} + 0.5\delta_R], \tag{5.12}$$

$$f^{A}_{C,\rm Int} \in [0.98 f^{A}_{T}, 1.02 f_{\rm peak}], \tag{5.13}$$

where $f_{\rm peak}$ is the analytical location of the peak of the Lorentzian describing the ringdown [15,16]

$$f_{\rm peak} = \left| f_{\rm RD} + f_{\rm damp}\sigma\frac{\sqrt{1-\lambda}-1}{\lambda}\right|. \tag{5.14}$$

The intermediate interval when building the waveform is defined by

$$f^{\varphi}_{\rm Int} \in [f_{\rm MECO} - \delta_R, f^{\varphi}_{T} + \delta_R] \tag{5.15}$$

$$f^{A}_{\rm Int} \in (f^{A}_{T}, f_{\rm peak}]. \tag{5.16}$$

The intermediate region corresponds to the green-shaded region in Fig. 4.

C. Merger-ringdown regime

Finally, the merger-ringdown regime is particularly well described in terms of the ringdown and damping frequency of the remnant BH. The calibration interval for the merger ringdown is taken to be

$$f^{\varphi}_{C,\rm MR} \in [0.985 f^{\varphi}_{T}, f_{\rm RD} + 1.25 f_{\rm damp}], \tag{5.17}$$

$$f^{A}_{C,\rm MR} \in \left[f_{\rm RD} - \frac{(1+4\eta)}{5} f_{\rm damp}, f_{\rm RD} + 3.25 f_{\rm damp}\right], \tag{5.18}$$

note that the factor of $(1+4\eta)$ has been added to help control the fits in the extreme-mass-ratio limit, where the amplitudes at the peak of the rescaled data can become particularly flat and no clear merger ringdown can be defined in a morphological sense.

The merger-ringdown frequency interval when reconstructing the waveform is defined by

$$f^{\varphi}_{\rm MR} \in (f^{\varphi}_{T}, 0.3Mf), \tag{5.19}$$

$$f^{A}_{\rm MR} \in (f_{\rm peak}, 0.3Mf), \tag{5.20}$$

where $0.3Mf$ is an arbitrary high-frequency cutoff frequency implemented for IMRPHENOMXAS in LAL. The merger-ringdown region corresponds to the blue-shaded region in Fig. 4.

VI. AMPLITUDE MODEL

When calibrating the amplitude model of IMRPHENOMXAS to the hybrid data, we factor out the leading order PN behavior $f^{-7/6}$. We opt to normalize the data such that as $f \to 0$ the data tends to unity. This normalization is motivated by the Newtonian limit

$$\lim_{f\to 0}[f^{7/6}A_{\rm PN}(f)] \to \sqrt{\frac{2\eta}{3\pi^{1/3}}}, \tag{6.1}$$

with the resulting normalization factor being

$$A_0 \equiv \sqrt{\frac{2\eta}{3\pi^{1/3}}} f^{-7/6}. \tag{6.2}$$

A. Inspiral

The inspiral model is based on a PN reexpanded TaylorF2 amplitude augmented with pseudo-PN terms that are calibrated to the hybrid data

$$A_{\rm Ins}(f) = A_{\rm PN} + A_0 \sum_{i=1}^{3} \rho_i (\pi f)^{(6+i)/3}, \tag{6.3}$$

where $A_{\rm PN}$ constitutes the known PN terms

$$A_{\rm PN}(f) = A_0 \sum_{i=0}^{6} \mathcal{A}_i (\pi f)^{i/3}, \tag{6.4}$$

and ρ_i are the *pseudo*-PN coefficients, where A_0 is the normalization factor corresponding to the leading order PN term $f^{-7/6}$. An example of the calibrated inspiral amplitude compared to the hybrid data is shown in Fig. 5.

The pseudo-PN coefficients are constructed by calibrating collocation points at the nodes

$$\{0.5, 0.75, 1.0\} f_{\rm MECO}, \tag{6.5}$$

and analytically solving the system of equations generated by evaluating the pseudo-PN terms in Eq. (6.3) at the above nodes.

B. Intermediate

As an example of the modularity of IMRPHENOMXAS, we implement two different models for the intermediate amplitude. The first model is based on the inverse of a fifth-order polynomial

$$A_{\rm Int} = \frac{A_0}{\alpha_0 + \alpha_1 f + \alpha_2 f^2 + \alpha_3 f^3 + \alpha_4 f^4 + \alpha_5 f^5}, \tag{6.6}$$

and the second model on the inverse of a fourth-order polynomial

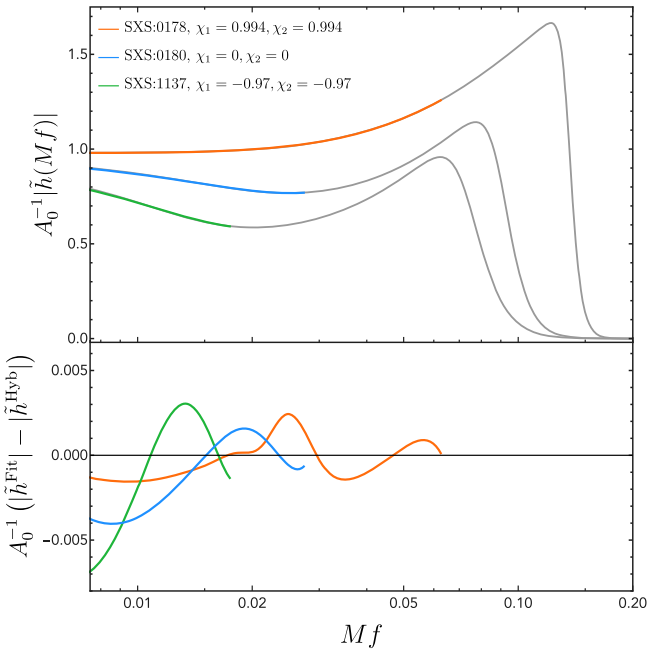

FIG. 5. The calibrated amplitude inspiral fit (blue curve) against a series of $q = 1$ SEOB-SXS NR hybrids (grey curves). The top panel shows the fit to the data and the bottom panel shows the residuals up to the $f_{\rm MECO}$ frequency.

$$A_{\rm Int} = \frac{A_0}{\alpha_0 + \alpha_1 f + \alpha_2 f^2 + \alpha_3 f^3 + \alpha_4 f^4}. \tag{6.7}$$

For an ansatz with n coefficients, we require n pieces of information in order to reconstruct the underlying function. For the fifth-order polynomial, the function requires six input parameters, given by the value of the amplitude at two collocation points together with four boundary conditions: two for the amplitude and two for the first derivative of the amplitude. The amplitude is therefore C^1 continuous by construction. A similar argument holds for the fourth-order function, though using 5 coefficients. The collocation points used for both models are detailed in Tables I and II. For the fifth-order polynomial, the coefficients α_i are the solution to the system of equations

TABLE I. Location of collocation points f_i for the fifth-order intermediate ansatz. The coefficients v_1, v_4, d_1, d_4 are constrained by the inspiral and merger-ringdown model. The free coefficients v_2 and v_3 must be fit to the data.

Collocation points	Value	Derivative
$f_1 = f_1^W$	$v_1 = A_{\rm Ins}(f_1)$	$d_1 = A'_{\rm Ins}(f_1)$
$f_2 = (f_T^A + f_{\rm peak})/3$	$v_2 = A_{\rm Hyb}(f_2)$	
$f_3 = 2(f_T^A + f_{\rm peak})/3$	$v_3 = A_{\rm Hyb}(f_3)$	
$f_4 = f_{\rm peak}$	$v_4 = A_{\rm MR}(f_4)$	$d_4 = A'_{\rm MR}(f_4)$

TABLE II. Location of collocation points f_i for the fourth-order intermediate ansatz. The coefficients v_1, v_3, d_1, d_3 are constrained by the inspiral and merger-ringdown model, whereas v_2 must be fit to the data.

Collocation points	Value	Derivative
$f_1 = f_T^A$	$v_1 = A_{\rm Ins}(f_1)$	$d_1 = A'_{\rm Ins}(f_1)$
$f_2 = (f_T^A + f_{\rm peak})/2$	$v_2 = A_{\rm Hyb}(f_2)$	
$f_3 = f_{\rm peak}$	$v_3 = A_{\rm MR}(f_3)$	$d_3 = A'_{\rm MR}(f_3)$

$$A_{\rm Ins}(f_1) = v_1, \tag{6.8}$$

$$A_{\rm Hyb}(f_2) = v_2, \tag{6.9}$$

$$A_{\rm Hyb}(f_3) = v_3, \tag{6.10}$$

$$A_{\rm MR}(f_4) = v_4, \tag{6.11}$$

$$A'_{\rm Ins}(f_1) = d_1, \tag{6.12}$$

$$A'_{\rm MR}(f_4) = d_4. \tag{6.13}$$

For the fourth-order polynomial, the system of equations is analogous to [16]

$$A_{\rm Ins}(f_1) = v_1, \tag{6.14}$$

$$A_{\rm Hyb}(f_2) = v_2, \tag{6.15}$$

$$A_{\rm MR}(f_4) = v_3, \tag{6.16}$$

$$A'_{\rm Ins}(f_1) = d_1, \tag{6.17}$$

$$A'_{\rm MR}(f_3) = d_3. \tag{6.18}$$

The fifth-order ansatz allows us to capture more dramatic features in the amplitude morphology, which is particular important as we extend to higher mass ratios. For aligned-spin binaries, the system is highly adiabatic and there are many quasicircular orbits before the smaller black hole plunges into the larger black hole. For antialigned spins, the system is not adiabatic and the system evolves through to the plunge phase much quicker, especially at high mass ratios. For the unadiabatic case, the binary shows a distinct morphology in which the amplitude drops as we rapidly transition from the inspiral to the merger ringdown. A comparison between the fourth-order and fifth-order intermediate ansatz against $q = 8$ hybrid data is shown in Fig. 6.

For the remainder of this paper, we will work with the fifth-order intermediate ansatz unless otherwise stated.

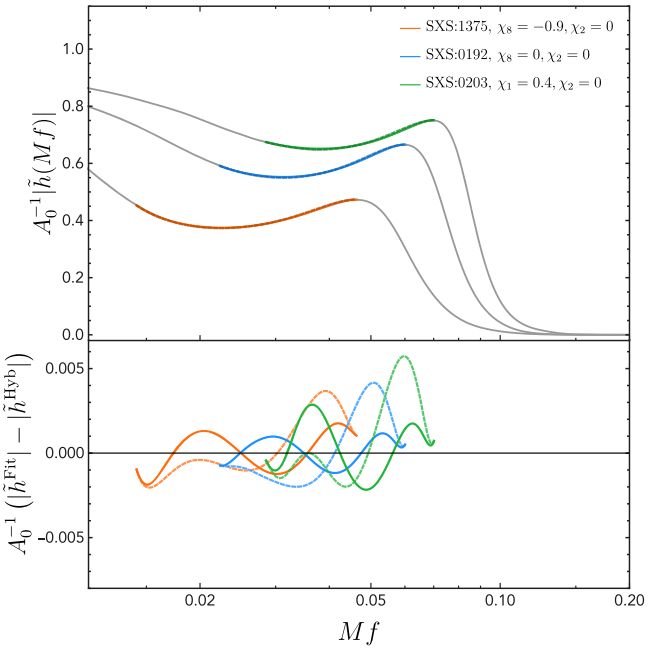

FIG. 6. The fit to the intermediate amplitude using a 4th-order (dashed curves) and 5th-order (solid curves) ansatz against 3 SXS simulations at $q = 8$ (grey curves). The 5th-order ansatz is able to more accurately fit the features in the waveform but has poor extrapolation compared to the 4th order ansatz. The top panel shows the direct fit to the data and the bottom panel the residuals.

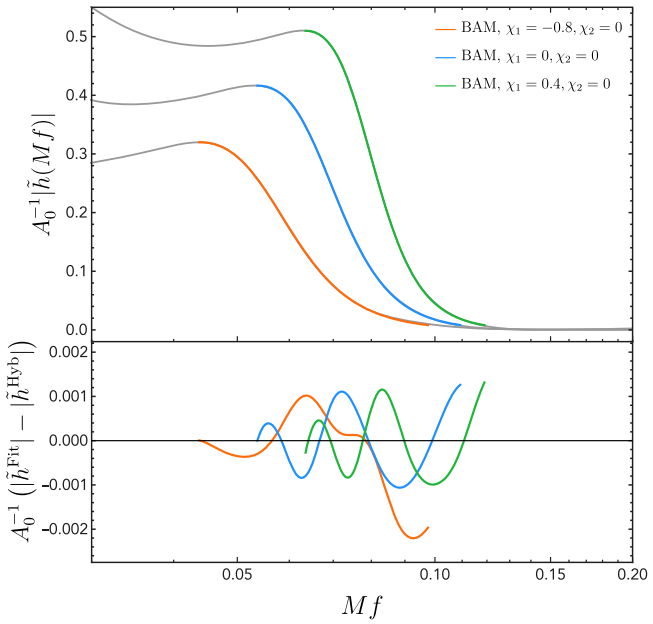

FIG. 7. The fit to the merger-ringdown amplitude for 3 BAM simulations at $q = 18$ corresponding to spins on the primary BH of $\chi_1 \in \{-0.8, 0, 0.4\}$. The secondary BH is nonspinning. The top panel shows the fit against the original hybrid data and the bottom panel the residuals.

C. Merger ringdown

The merger-ringdown ansatz is modeled using a deformed Lorentzian, corresponding to the Fourier transform of a two-sided exponential decay function. The ansatz adopted is given by [15,16]

$$A_{\rm MR} = \left[\frac{a_R(f_{\rm damp}\sigma)}{(f-f_{\rm RD})^2+(f_{\rm damp}\sigma)^2}\right] e^{-\lambda(f-f_{\rm RD})/(f_{\rm damp}\sigma)}. \quad (6.19)$$

Unlike the other two regions, here we choose to calibrate λ and σ directly. By this we simply mean that we produce a hierarchical fit to the value of the phenomenological coefficient across the binary parameter space rather than fitting to the value of the amplitude at the collocation points and solving the resulting system of linear system equations, as in Eq. (4.3). In order to solve the amplitude coefficient a_R, we further calibrate a collocation point at the defined at $f_{\rm peak}$. Together with λ and σ, we can use the collocation point to solve a trivial system of equations for a_R. An example of the ringdown fit applied to the BAM $q = 18$ data is shown in Fig. 7.

VII. PHASE MODEL

A. Inspiral

The inspiral phase model is based on TaylorF2, derived under the stationary phase approximation, augmented with pseudo-PN coefficients that are calibrated to the hybrid data. We write out inspiral phase as

$$\begin{aligned}\varphi_{\rm Ins} &= \varphi_{\rm TF2}(Mf;\boldsymbol{\theta}) \\ &+\frac{1}{\eta}\left(\sigma_0+\sigma_1(Mf)+\frac{3}{4}\sigma_2(Mf)^{4/3}+\frac{3}{5}\sigma_3(Mf)^{5/3}\right. \\ &\left.+\frac{1}{2}\sigma_4(Mf)^{6/3}+\frac{3}{7}\sigma_5(Mf)^{7/3}\right). \end{aligned} \quad (7.1)$$

where $\varphi_{\rm TF2}$ is the analytically known TaylorF2 phase

$$\begin{aligned}\varphi_{\rm TF2} &= 2\pi f t_c-\varphi_c-\frac{\pi}{4} \\ &+\frac{3}{128\eta}(\pi Mf)^{-5/3}\sum_{i=0}^{7}\varphi_i(\boldsymbol{\theta})(\pi Mf)^{i/3}, \end{aligned} \quad (7.2)$$

and $\varphi_i(\boldsymbol{\theta})$ are known PN coefficients that are functions of the intrinsic parameters of the binary, see Appendix A. The coefficients σ_i are the pseudo-PN coefficients that we calibrate against the hybrid dataset and supplementary SEOBNRv4 waveforms. A detailed discussion of the PN information used in IMRPHENOMXAS is given in Appendix A.

The calibration of the pseudo-PN coefficients is performed by subtracting a given TaylorF2 approximant from the full hybrid phase and factoring out the leading order frequency power

$$\mathcal{R}_{\rm insp}(Mf) = (Mf)^{-8/3}(\varphi'_{\rm Hybrid}(Mf)-\varphi'_{\rm TF2}(Mf)). \quad (7.3)$$

where $' = \partial_f$. By performing such a rescaling, we numerically condition the data such that we more accurately capture the un-modeled higher-PN contributions to the phase.

Note that, by construction, the calibrated pseudo-PN coefficients are implicitly tied to the specific TaylorF2 approximant used. If we incorporate additional analytical PN information, we would need to recalibrate the pseudo-PN coefficients on a case-by-case basis.

In this paper, we demonstrate the flexibility of the IMRPHENOMXAS framework by producing four different calibrated inspiral models. The first two models adopt a *canonical* 3.5PN TaylorF2 phase using recent cubic-in-spin and quadratic-in-spin corrections [106,107] but use 4 or 5 pseudo-PN coefficients, with σ_0 being fixed by imposing C^1 continuity in the phase. The model with 4 additional coefficients requires 4 collocation points whereas the model with 5 additional coefficients requires 5 collocations points. The final set of models are all based on an *extended* TaylorF2 phase that incorporates some recent results at 4PN [108–113], 4.5PN [114] and a recently identified

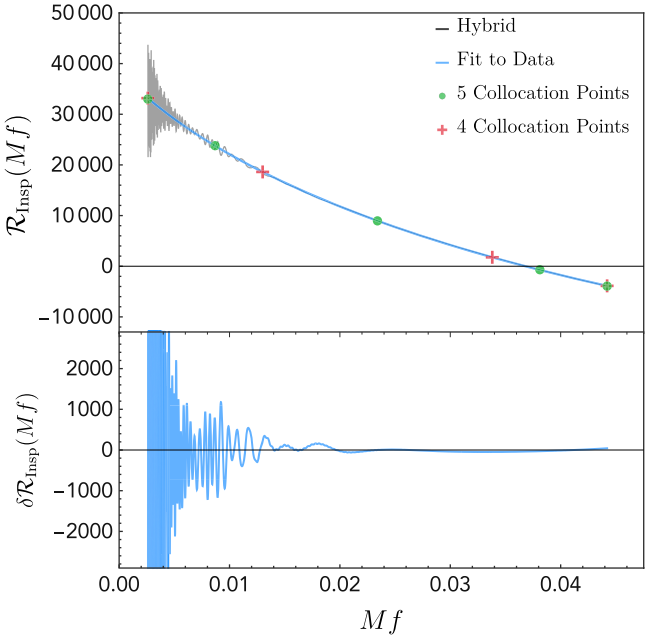

FIG. 8. The pseudo-PN coefficients are fit to the hybrid data by subtracting a given TaylorF2 approximant and factoring out the leading order frequency, $f^{-8/3}[\varphi'_{\rm Hyb}(f)-\varphi'_{\rm TF2}(f)]$. Such data conditioning helps improve the accuracy of the fit up to the MECO frequency. The green circles denote the location of the nodes when using 5 collocation points and the red crosses for 4 collocation points. The sampling points are chosen based on a Gauss-Chebyshev scheme aimed at reducing Runge's phenomena near the boundaries. The SEOB-NR hybrid shown is for SXS:0153, a binary with $q = 1$ and $\chi_1 = \chi_2 = 0.85$. The top panel shows the direct fit to the data and the bottom panel the residuals of the fit, $\delta\mathcal{R} = \mathcal{R}^{\rm Fit}_{\rm Insp} - \mathcal{R}^{\rm Hyb}_{\rm Insp}$.

tail-induced, spin-spin term in the flux [95]. As before, we produce two variants with 4 and 5 pseudo-PN coefficients respectively.

The collocation points for this system are set by the Gauss-Chebyshev nodes. When using 4 collocation points, these nodes are given by

$$v_i^{\rm Int} = M\left\{f_L, \frac{1}{4}\delta_\varphi^{\rm Im}, \frac{3}{4}\delta_\varphi^{\rm Im}, f_H\right\} \tag{7.4}$$

where $f_H = 1.02 f_{\rm MECO}$, $f_L = 0.0026$ and $\delta_\varphi^{\rm Im} = f_H - f_L$. For 5 collocation points, the nodes occur at

$$v_i^{\rm Int} = M\left\{f_L, \frac{1}{2}\left(1-\frac{1}{\sqrt{2}}\right)\delta_\varphi^{\rm Im} + f_L, f_L + \frac{1}{2}\delta_\varphi^{\rm Im}, \frac{1}{2}\left(1+\frac{1}{\sqrt{2}}\right)\delta_\varphi^{\rm Im} + f_L, f_H\right\}. \tag{7.5}$$

The location of the nodes when using 4 and 5 collocation points is demonstrated in Fig. 8, where we fit the residual ansatz in Eq. (7.3) to the hybrid data.

Unless otherwise stated, we adopt the *canonical* TaylorF2 ansatz with *4 pseudo-PN coefficients* as the default inspiral model. The performance of the different inspiral models is discussed in Sec. IX and the mismatches, as defined in Eq. (9.1), shown in Fig. 17. The low-frequency oscillations occur due to numerous artifacts including residual eccentricity and numerical conditioning from the Fourier transforms. We note that these oscillations are overly pronounced due to the scaling by $f^{-8/3}$ and seemingly have little impact on the quality of the fit.

B. Intermediate

We now consider the phenomenological intermediate region. As in [15,16], we adopt a polynomial ansatz but add a Lorentzian term to smoothly match the phase to the merger-ringdown ansatz. As with the inspiral, we provide two models as an example of the modularity of IMRPHENOMXAS. The functional form for the general ansatz used for the intermediate phase is

$$\eta\varphi'_{\rm Int} = \beta_0 + \beta_4 f^{-4} + \beta_3 f^{-3} + \beta_2 f^{-2} + \beta_1 f^{-1} - \frac{4 c_0 a_\varphi}{(f - f_{\rm RD})^2 + (2 f_{\rm damp})^2}, \tag{7.6}$$

where the Lorentzian term, i.e., the nonpolynomial coefficient, is fixed by the merger-ringdown model. The first model adopts 4 collocation points and sets $\beta_3 = 0$. The second model uses 5 collocation points, retaining all 5 coefficients $\{\beta_0, \beta_1, \beta_2, \beta_3, \beta_4\}$. Unlike IMRPHENOMD, we impose additional constraints on the intermediate ansatz and use the value of the inspiral and merger-ringdown fits respectively to determine the boundary collocation points. The 4-coefficient model therefore requires two calibrated collocation points and the 5-coefficient model 3 calibrated terms. The Gauss-Chebyshev nodes for 4 collocation points occur at

$$v_i^{\rm Int} = \left\{f_L, \frac{1}{4}\delta_\varphi^{\rm Im}, \frac{3}{4}\delta_\varphi^{\rm Im}, f_H\right\}, \tag{7.7}$$

where $f_H = f_T^\varphi + 0.5\delta_R$, $f_L = f_{\rm MECO} - \delta_R$ and $\delta_\varphi^{\rm Im} = f_H - f_L$. Similarly, for the 5 collocation points, the nodes occur at

$$v_i^{\rm Int} = \left\{f_L, \frac{1}{2}\left(1-\frac{1}{\sqrt{2}}\right)\delta_\varphi^{\rm Im} + f_L, f_L + \frac{1}{2}\delta_\varphi^{\rm Im}, \frac{1}{2}\left(1+\frac{1}{\sqrt{2}}\right)\delta_\varphi^{\rm Im} + f_L, f_H\right\}. \tag{7.8}$$

In order to help numerically condition the collocation points, we opted to fit the difference with respect to $v_4^{\rm MR}$, the value of the merger-ringdown phase at the ringdown frequency. Such a strategy is particularly beneficial when extrapolating to higher mass ratios and high-spin configurations, where the sparsity of available NR simulations can lead to poor constraints on the parameter space fits. For the 4-coefficient model, the two free coefficients are v_2 and v_3. We therefore require parameter space fits for

$$\delta_{2,\rm RD4} = v_2^{\rm Im} - v_4^{\rm RD}, \tag{7.9}$$

$$\delta_{3,\rm RD4} = v_3^{\rm Im} - v_4^{\rm RD}, \tag{7.10}$$

which could be used in conjunction with a fit for $v_4^{\rm RD}$ to reconstruct $v_2^{\rm Im}$ and $v_3^{\rm Im}$ respectively. In order to help tame unphysical behavior at extremely large mass ratios and large spins, we use a weighted average between the fit to the differences, as above, and a direct fit to the collocation point $\bar{v}_2^{\rm Im}$ in the final model

$$v_2^{\rm Im} = \frac{3}{4}(\delta_{2,\rm RD4} + v_4^{\rm RD}) + \frac{1}{4}\bar{v}_2^{\rm Im}. \tag{7.11}$$

An example of the reconstructed intermediate phase derivative against hybrid data, along with the collocation points used, is shown in Fig. 9. Unless otherwise stated, we take the 5th order polynomial ansatz as the default model for the intermediate phase derivative.

C. Merger ringdown

As in previous phenomenological waveform models, the ansatz for the merger ringdown is based on a Lorentzian embedded in a background arising form the late inspiral and merger. In order to capture the steep inspiral gradient, negative powers of the frequency were added to the Lorentzian

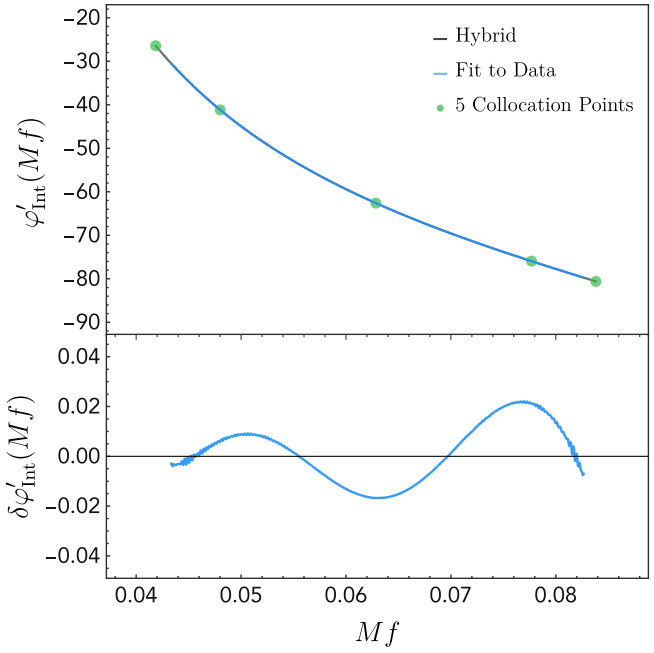

FIG. 9. Phase derivative of the EOB-NR hybrid using SXS-BBH-0153, as in Fig. 8. Here we show the intermediate hybrid data (gray curve) and the corresponding fit to the data (blue) reconstructed from a system of collocation points (green). The top panel shows the direct fit to the data and the bottom panel the residuals of the fit, $\delta\varphi' = \varphi'_{\rm Int,Fit} - \varphi'_{\rm Int,Hyb}$.

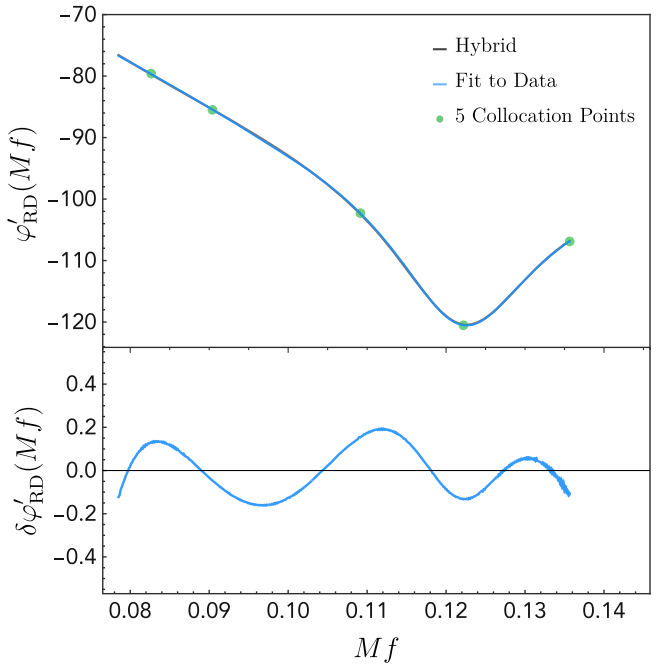

FIG. 10. Phase derivative for the EOB-NR hybrid using SXS-BBH-0153, as in Fig. 8. Here we show the hybrid merger ringdown (gray curve) along with the fit to the data (blue) reconstructed from the system of collocation points (green). The top panel shows the direct fit to the data and the bottom panel the residuals of the fit, $\delta\varphi' = \varphi'_{\rm RD,Fit} - \varphi'_{\rm RD,Hyb}$.

$$\eta\varphi'_{\rm RD} = c_{\rm RD} + \sum_i^n c_i f^{-p_i} + \frac{c_0 a_\varphi}{f_{\rm damp}^2 + (f - f_{\rm RD})^2}. \quad (7.12)$$

In IMRPHENOMD, the leading contribution was taken to be $p_2 = 2$ and an additional term $p_3 = -1/4$ was added in order to reduce residuals across the parameter space. However, for IMRPHENOMXAS, we find that we no longer require the coefficient α_5, defined in Eq. (13) of [16], to correct for the ringdown frequency. Using the recent recalibration of the final mass and spin fits in [25], the values of the ringdown and damping frequency are sufficiently accurate that we are able to drop this coefficient. This allows us to calibrate an additional coefficient without increasing the dimensionality of the fit. The inclusion of an additional polynomial coefficients is of particular importance in correctly modeling the gradient of the merger ringdown in the extremal spin limit. For IMRPHENOMXAS, we use three polynomial coefficients with powers of -4, -2 and $-1/3$ respectively.

As with the other regions, we use Gauss-Chebyshev nodes to fix the collocation points but set the 4th node to occur at the ringdown frequency. The ringdown frequency approximately correponds to the peak of the Lorentzian, as can be seen in Fig. 10. Whilst this may impact the optimality of reconstructing the underlying function, we find that $v_4^{\rm MR}$ is very well conditioned and can be fit to high accuracy. The collocation points nodes for the merger-ringdown phase are therefore taken to be

$$v_i = M\left\{f_L, \frac{1}{2}\left(1 - \frac{1}{\sqrt{2}}\right)\delta_\varphi^{\rm MR} + f_L, f_L + \frac{1}{2}\delta_\varphi^{\rm MR}, f_{\rm RD}, f_H\right\}, \quad (7.13)$$

where $f_H = f_{\rm RD} + \frac{5}{4} f_{\rm damp}$, $f_L = f_T^\varphi$ and $\delta_\varphi^{\rm MR} = f_H - f_L$.

An example of the reconstructed merger-ringdown phase derivative against hybrid data, along with the collocation points used, is shown in Fig. 10. The fit detailed here is as implemented in the final model.

D. Final state

Accurate modeling of the final state is important as this determines the ringdown $f_{\rm RD}$ and damping $f_{\rm damp}$ frequencies that enter into the amplitude and phase model, e.g., see Eq. (6.19) and (7.12). Notably, the ringdown $f_{\rm RD}$ and damping $f_{\rm damp}$ frequencies determine the peak and shape of the Lorentzian ringdown for the amplitude and phase. IMRPHENOMXAS implicitly benefits from the improved recalibration of the final state fits presented in [25]. Due to these improvements, we find that we no longer require α_5 in [16], which was introduced to correct for deficiencies in modeling the final state.

The total angular momentum can be written in terms of the physical spins $\vec{S}_1$, $\vec{S}_2$ and the orbital angular momentum $\vec{L}$ as

$$\vec{J} = \vec{L} + \vec{S}_1 + \vec{S}_2, \tag{7.14}$$

where $\vec{S}_i$ change negligibly in the aligned-spin limit. Due to the symmetry of the binary, all vector components orthogonal to the orbital angular momentum vanish and we are only left with components in the z-direction. For brevity, we drop the vector notation as we are only dealing with the z-components. Given that Eq. (7.14) depends on the total spin $S_{\rm tot} = S_1 + S_2$, it is reasonable to expect that the final BH spin

$$\chi_f = J_f/M_f^2, \tag{7.15}$$

will be well approximated by $J_f \approx J(\eta, S_{\rm tot}, \Delta\chi)$, motivating the use of $S_{\rm tot}$ as the spin-parametrization of choice for the final state. A detailed discussion of the final state fits used in IMRPHENOMXAS is given in [25].

In order to determine the dimensionless ringdown and damping frequencies as a function of χ_f, we fit a rational function to the data set in [115]. To calculate the dimensionful ringdown frequency, we must also take into account energy loss during the inspiral

$$\frac{2\pi f_{\rm RD} M}{M_f} = \frac{2\pi f_{\rm RD} M}{M - E_{\rm rad}}, \tag{7.16}$$

where $E_{\rm rad}$ is determined using the fit in [25]. A similar expression holds for the damping frequency.

VIII. MODEL CALIBRATION, A WORKED EXAMPLE

In this section we provide a worked example of the hierarchical fitting procedure used to calibrate IMRPHENOMXAS. Here we detail the calibration of $v_4^{\rm MR}$, the value of the phase derivative of the EOB-NR hybrids evaluated at the ringdown frequency, effectively describing the phase derivative at the peak of the Lorentzian. We use available SXS, BAM and ET waveforms supplemented by the test-particle waveforms. As was also observed in [15,25], an effective spin parametrization defined in terms of the dimensionful spin components S_i most accurately reflects the physics driving the merger ringdown. The spin parametrization, $\hat{S}$, that we will use to calibrate $v_4^{\rm MR}$ is the total effective spin, $\hat{S}_{\rm tot}$, defined in Eq. (4.18).

A. 1D Fits

The starting point for the hierarchical fitting procedure is a 1D fit to the value of the collocation point $v_4^{\rm MR}$ for the nonspinning EOB-NR hybrids. We follow the general procedure of first producing a high-degree polynomial and using this to construct a Padé approximant that can be used to pre-condition a rational fit using the `NonLinearModelFit` package in *Mathematica*. The resulting rational function fit is of the following form

$$F(\eta) = \frac{a_0 + a_1\eta + a_2\eta^2 + a_3\eta^3 + a_4\eta^4 + a_5\eta^5}{1 + a_6\eta}, \tag{8.1}$$

with numerical coefficients

$$\begin{aligned} a_0 &= -85.8606, \\ a_1 &= -4616.74, \\ a_2 &= -4925.76, \\ a_3 &= 7732.06, \\ a_4 &= 12828.3, \\ a_5 &= -39783.5, \\ a_6 &= 50.2063. \end{aligned} \tag{8.2}$$

We now follow the same procedure to generate a fit to the 1D equal-mass, equal-spin hybrid data. In terms of an effective spin parametrization $\hat{S}$, we obtain a rational fit of the form

$$F(\hat{S}) = b_0 + \frac{b_1\hat{S} + b_2\hat{S}^2 + b_3\hat{S}^3 + b_4\hat{S}^4 + b_5\hat{S}^5}{1 + b_6\hat{S}}, \tag{8.3}$$

with numerical coefficients

$$\begin{aligned} b_0 &= -104.477, \\ b_1 &= -19.0379, \\ b_2 &= 15.3476, \\ b_3 &= -0.419939, \\ b_4 &= -0.884176, \\ b_5 &= -0.631487, \\ b_6 &= -0.729629. \end{aligned} \tag{8.4}$$

This fit has been constrained by imposing the limit $F(\hat{S} = 0) = F(\eta = 0.25)$, ensuring that there are no discontinuities between $F(\hat{S})$ and $F(\eta)$ in the limit $\hat{S} \to 0$. Figures 11 and 12 show the 1D fits for the nonspinning and equal-mass, equal-spin subspaces respectively. The top panels show the direct fits to the data along with the 90% confidence levels estimated using `NonLinearModelFit`. The bottom panels show the residuals between the 1D fits and the hybrid data.

B. 2D fits

The two-dimensional fits to the $(\eta, \hat{S})$ subspace are constructed by combining both of the 1D subspace fits

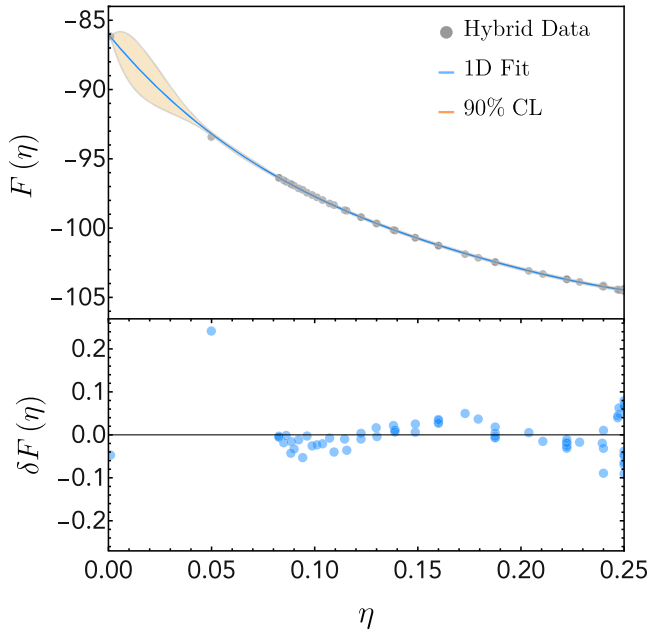

FIG. 11. The 1D fit to the nonspinning hybrid data, Eq. (8.1). The blue curves show the 1D fit to the data and the orange shaded region denotes the 90% confidence level for the fit. The grey points denote the input NR and test-particle data. The nonspinning parameter space is densely covered up to $q \sim 10$ with only the nonspinning BAM simulation at $q = 18$. Whilst test-particle data can be used to constrain the fit in the extreme-mass-ratio limit boundary $q \sim 10^3$, there is a clear degree of uncertainty in the fit at mass ratios $q > 20$. The top panel shows the direct fit and the bottom panel shows the residuals.

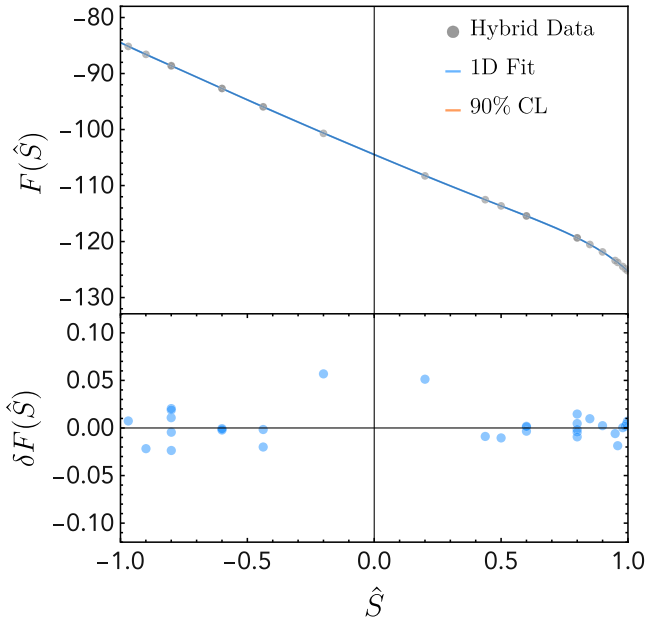

FIG. 12. The 1D fit to the equal-mass equal-spin hybrid data, Eq. (8.3). The blue curves show the 1D fit to the data and the orange shaded region denotes the 90% confidence level for the fit. The grey points denote the input NR and test-particle data. Unlike the nonspinning subspace, the equal-mass and equal-spin region of the parameter space is exceptionally well constrained and the 90% confidence level is indistinguishable from the direct fit.

derived above. As discussed in Sec. IV C, we generalize the $\hat{S}$-dependent fits by inserting a polynomial of order J in η for each coefficient in the 1D fit [25,88]. Here we opt to use a fourth order in η expansion ($J = 4$) and kill the least constrained coefficients (i.e., p-values near unity) as determined by the nonlinear model fit. In addition, we fix all coefficients on the denominator to avoid singularities. The constrained 2D fit $F(\eta, \hat{S})$ against the input data is shown in Fig. 13.

C. Full 3D fits

The final step in the procedure is to fit the unequal spin effects, parametrized by $\Delta\chi = \chi_1 - \chi_2$, to the residual data, as discussed in Sec. IV D. In Fig. 14, we show the unequal spin subspace for all $q = 3$ NR data. As anticipated, the data is dominated by a linear-in-spin-difference terms with only weak evidence for higher order corrections. Fits are performed at all mass ratios for which we have sufficient data to constrain the ansatz. Note that the ansatz per-mass-ratio is used to inform the full 3D ansatz and as a consistency check. The 3D fit implemented in the model is constructed by fitting the constrained 2D ansatz plus the unequal spin terms to the full NR dataset. Here we demonstrate two approaches to constraining the unequal-spin fit. In the first approach, we restrict our analysis to the linear-in-spin-difference term $\Delta\chi$

$$\Delta v_4^{\rm MR}(\eta, \hat{S}, \Delta\chi) = A_1(\eta)\Delta\chi. \tag{8.5}$$

In the second approach we use the full quadratic in unequal spin-correction ansatz

$$\Delta v_4^{\rm MR}(\eta, \hat{S}, \Delta\chi) = F^{\rm Lin}(\eta)\Delta\chi + F^{\rm Quad}(\eta)\Delta\chi^2 + F^{\rm Mix}(\eta)\hat{S}\Delta\chi. \tag{8.6}$$

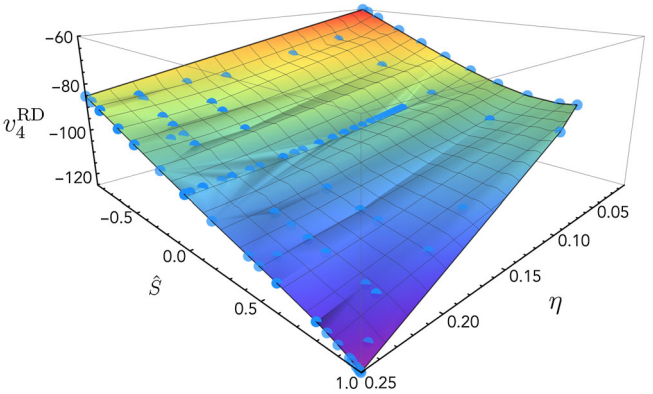

FIG. 13. Fit $F(\eta, \hat{S})$ to the two-dimensional subspace $\{\eta, \hat{S}\}$. The blue points denote NR and test-particle data.

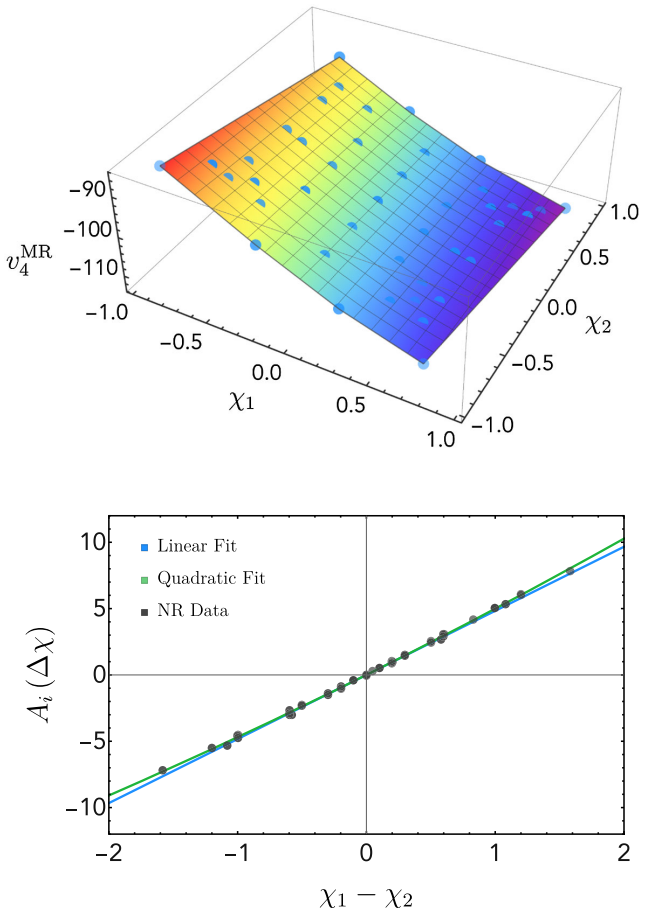

FIG. 14. Example of the spin-difference behavior at a mass ratio $q = 3$. At such mass ratios the surface is very close to flat and the linear-in-spin difference term dominates. The A_i denote the linear in spin-difference and quadratic in spin-difference coefficients defined in Eq. (4.13).

Based on the symmetry arguments outlined in [25,88] and Sec. IV D, we adopt an ansatz for the linear in spin-difference term of the form

$$F^{\rm Lin}(\eta) = d_{10}\eta(1 + d_{11})\sqrt{1 - 4\eta}. \tag{8.7}$$

For the quadratic in spin-difference and mixed spin-difference ansätze, we adopt simpler fits of the form

$$F^{\rm Quad}(\eta) = d_{20}\eta, \tag{8.8}$$

$$F^{\rm Mix}(\eta) = d_{30}\eta\sqrt{1 - 4\eta}. \tag{8.9}$$

Whilst more complicated ansätze could be pursued, we typically find that the systematic errors in the NR data and strong correlations lead to poor constraints on the coefficients. As can be seen in the top two plots of Fig. 15, the shape and numerical value of the linear term is robust when adding different combinations of the unequal spin terms. Applying the fits to all data, we find

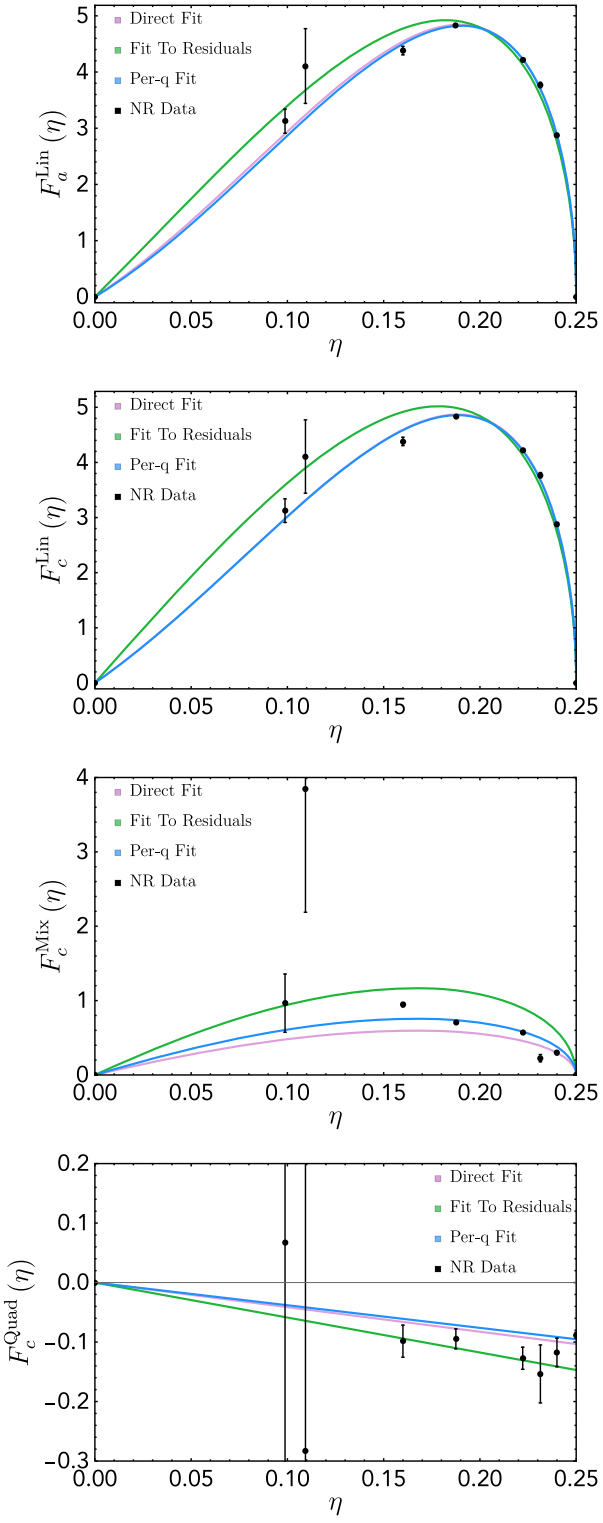

FIG. 15. Fits to the unequal spin data. The first plot shows the linear-in-spin difference fit. The second plot shows the linear-in-spin difference contribution to the full unequal spin ansatz in Eq. (4.13), $f_c^{\rm Lin}(\eta)\Delta\chi$ fit. The third plot the mixed-spin fit $f_c^{\rm Mix}(\eta)\hat{S}\Delta\chi$ and the final plot shows the quadratic in spin-difference fit $f_c^{\rm Quad}(\eta)(\Delta\chi)^2$. Whilst the linear-in-spin difference is relatively well captured, the second order unequal spin effects are less resolved with the coefficients for the fits becoming poorly constrained.

$$d_{10} = 22.3632, \tag{8.10}$$

$$d_{11} = 6.9794, \tag{8.11}$$

for the linear-only ansatz and

$$d_{10} = 24.1579, \tag{8.12}$$

$$d_{11} = 6.1330, \tag{8.13}$$

$$d_{20} = -0.4132, \tag{8.14}$$

$$d_{30} = 6.1896 \tag{8.15}$$

for the full ansatz. Though the data shows some evidence for quadratic-in-spin-difference corrections, third plot of Fig. 15, and mixed spin-difference terms, second plot of Fig. 15, systematic errors prevent a robust fit to the data. As such, for IMRPHENOMXAS we opt to use the linear-only ansatz in the final 3D fit.

The full 3D fit to the hybrid data is

$$\begin{aligned}\Delta v_4^{\rm MR}(\eta,\hat{S},\Delta\chi) = {} & \frac{a_0 + a_1\eta + a_2\eta^2 + a_3\eta^3 + a_4\eta_4 + a_5\eta_6}{1 + a_6\eta} + \frac{1}{1 + b_6\hat{S}}[\hat{S}(c_0 + c_1\eta + c_2\eta^2 + c_3\eta^3 + c_4\eta^4) \\ & + \hat{S}^2(d_0 + d_1\eta + d_2\eta^2 + d_3\eta^3 + d_4\eta^4) + \hat{S}^3(e_0 + e_1\eta + e_2\eta^2 + e_3\eta^3 + e_4\eta^4) \\ & + \hat{S}^4(f_0 + f_1\eta + f_2\eta^2 + f_3\eta^3 + f_4\eta^4) + \hat{S}^5(g_0 + g_1\eta + g_2\eta^2 + g_3\eta^3 + g_4\eta^4)] + h_0(1 + h_1\eta)\sqrt{1-4\eta}\Delta\chi,\end{aligned} \tag{8.16}$$

where $\Delta v_4^{\rm MR}$ is the value of the merger-ringdown phase at the ringdown frequency. This collocation point effectively captures the value of the phase derivative at the peak of the Lorentzian, e.g., Eq. (7.12). The coefficients a_i are defined in Eqs. (8.2) and b_6 in Eq. (8.4). The additional coefficients are

$$\begin{aligned} c_0 &= -24.32, & c_1 &= 50.49 \\ c_2 &= -68.32, & c_3 &= 0.0 \\ c_4 &= 784.98 & & \\ d_0 &= 26.62, & d_1 &= -19.39 \\ d_2 &= 13.27, & d_3 &= 1092.51 \\ d_3 &= 2512.13, & & \\ e_0 &= 2.80, & e_1 &= 11.23 \\ e_2 &= -308.99, & e_3 &= 74.22 \\ e_4 &= 3103.82, & & \\ f_0 &= -1.68, & f_1 &= -22.78 \\ f_2 &= 76.14, & f_3 &= 0.0 \\ f_4 &= 443.83, & & \\ g_0 &= -1.21, & g_1 &= -71.28 \\ g_2 &= 525.24, & g_3 &= 0.0 \\ g_4 &= 3694.97, & & \\ h_0 &= 22.36, & h_1 &= 6.98. \end{aligned}$$

The full 3D fits for all coefficients required for IMRPHENOMXAS are given in the Supplementary Material [116] attached to this paper.

IX. MODEL VALIDATION

A. Mismatches against hybrid dataset

The agreement between two waveforms h_1 and h_2 can be quantified by the overlap, the noise-weighted inner product

$$\langle h_1, h_2\rangle = 4\mathrm{Re}\int_{f_{\rm min}}^{f_{\rm max}} \frac{\tilde{h}_1(f)\tilde{h}_2^*(f)}{S_n(f)}df. \tag{9.1}$$

The *match* is defined as the normalised ($\hat{h} = h/\sqrt{\langle h, h\rangle}$) inner product maximized over time and phase shifts

$$M(h_1, h_2) = \max_{t_0,\phi_0}\langle \hat{h}_1, \hat{h}_2\rangle. \tag{9.2}$$

The *mismatch* is then defined as

$$\mathcal{M}(h_1, h_2) = 1 - M(h_1, h_2). \tag{9.3}$$

In all matches presented here, we use the zero-detuned high-power (zdethp) PSD [117,118]. We use a low frequency cutoff of 20 Hz and an upper cutoff frequency of 8192 Hz.

In order to assess the accuracy of our model, we compute the mismatch against all SXS hybrids produced for IMRPHENOMXAS. As shown in Fig. 16, IMRPHENOMXAS shows 1 to 2 orders of magnitude improvement over IMRPHENOMD across the entire parameter space. Figure 17 shows mass-averaged mismatches for the performance of the four calibrated inspiral models discussed in Sec. VII A. As we focus on the dominant-mode nonprecessing waveforms, we neglect all extrinsic BBH parameters, such as orientation or sky-location, in our mismatch. The inclusion of additional pseudo-PN coefficients demonstrates mild performance

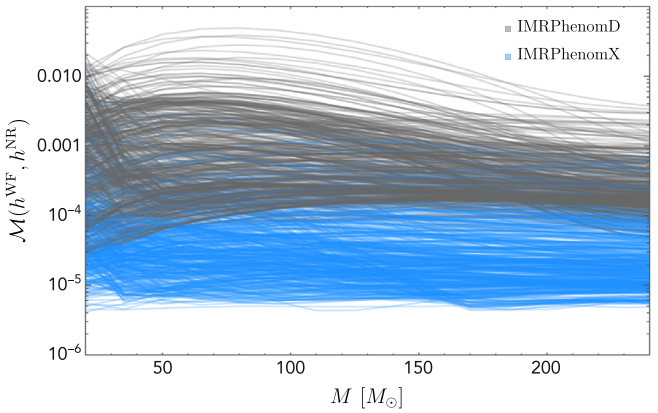

FIG. 16. Mismatches for IMRPHENOMXAS (blue) and IMRPHENOMD (grey) against all SXS NR hybrids. We use the Advanced LIGO design sensitivity PSD and a lower frequency cutoff of 20 Hz. We see a dramatic decrease in the mismatch by 1 to 2 orders of magnitude across the parameter space.

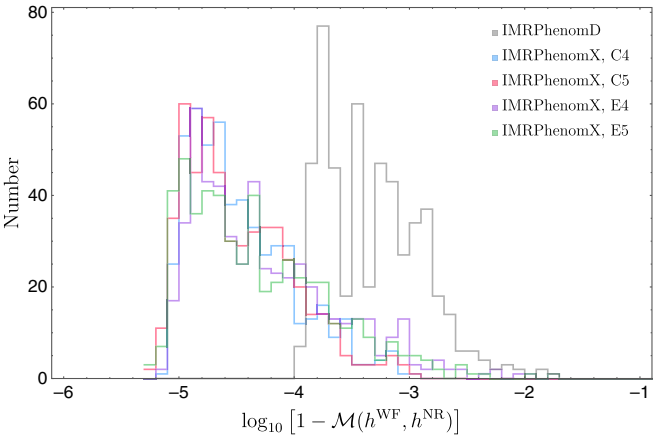

FIG. 17. Mass averaged mismatches in a range of 20–250 $M_\odot$ for IMRPHENOMXAS and IMRPHENOMD against all SXS NR hybrids. We use the Advanced LIGO design sensitivity PSD and a lower frequency cutoff of 20 Hz. We showcase four variants of IMRPHENOMXAS corresponding to different inspiral models. The C denotes the canonical TaylorF2 baseline at 3.5PN and the E denotes the extension to 4PN and 4.5PN order discussed in the Appendix. The number, 4 or 5, denotes the number of pseudo-PN terms used in the model.

improvements, though not at a significantly appreciable level. We note that the small tails visible for versions E4 and E5 could be further improved with further refinement to the calibration pipeline, as was done for versions C4 and C5. In Fig. 18 we show mismatches for IMRPHENOMXAS, IMRPHENOMD and SEOBNRV4_ROM against NRHybSur3dq8 [119] for mass ratios below 9.09 and dimensionless spin magnitudes up to 0.8.

B. Time domain conversion

Although IMRPHENOMXAS is expressed in terms of closed-form frequency domain expressions, the input

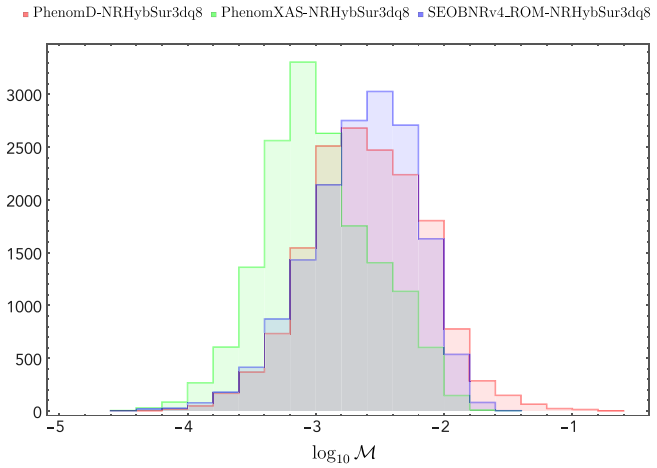

FIG. 18. The $(\ell, m) = (2, 2)$ mismatches $\mathcal{M}$ for IMRPHENOMXAS (green), IMRPHENOMD (red), and SEOBNRV4 (blue) against NRHybSur3dq8, the NR hybrid surrogate valid up to a mass ratio $q = 8$ and spins $\chi_i = \pm 0.8$. We compute the matches at random points in the parameter space, including points that fall between the calibration datasets used to construct IMRPHENOMXAS. Here we clearly see that IMRPHENOMXAS offers a significant improvement in performance in comparison to IMRPHENOMD or SEOBNRV4.

calibration data and output from NR are time-domain function. It is therefore useful and illustrative to check the behavior of the model when transformed from the frequency-domain back to the time-domain via an inverse Fourier transformation. In particular, the model should be a smooth function in both the frequency- and time-domain. Such comparisons are often useful as an additional consistency check on the physical accuracy of the model. In Fig. 19 we plot the time-domain reconstruction of IMRPHENOMXAS against selected SXS or BAM waveforms at the boundary of the calibration region for NR. We find excellent agreement between IMRPHENOMXAS and input NR data, even when considering near extremal spin configurations (first panel) as well as at large mass ratios and relatively large spins (last two panels). Note that we have optimized over a time and phase shift when aligning the waveforms. Such comparisons provide further evidence, in addition to the mismatches, that our end-to-end pipeline for hybridization, calibration, and model reconstruction are faithfully reproducing the input data.

As in [16], the frequency domain data is tapered and an optimal sampling rate chosen through the stationary phase approximation.

C. Parameter estimation

1. GW150914

As an example of the application of IMRPHENOMXAS to gravitational-wave data, we reanalyze GW150914 and demonstrate broad agreement between IMRPHENOMXAS,

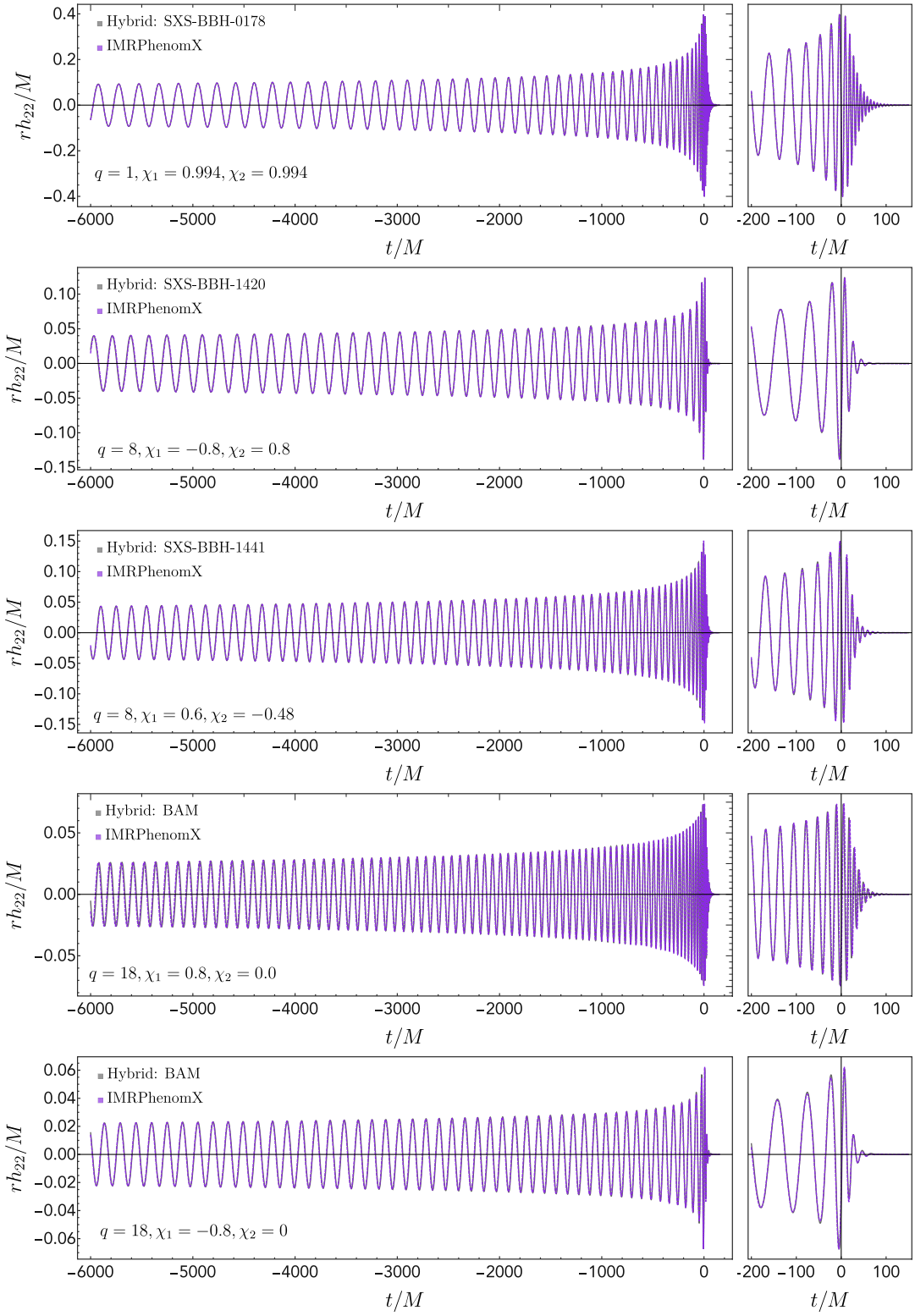

FIG. 19. Time-domain IMRPHENOMXAS waveforms (violet) and SEOBNRv4-NR hybrids (grey) for configurations at the edge of the calibration domain.

IMRPHENOMD and SEOBNRv4. We use coherent Bayesian inference methods to determine the posterior distribution $p(\vec{\theta}|\vec{d})$ for the parameters that characterize the binary. We use the nested sampling algorithm implemented in LALINFERENCE [3] and the public data from the Gravitational Wave Open Science Center (GWOSC)

[120–122]. Following [7], we marginalize over the frequency dependent spline calibration envelopes that characterize the uncertainty in the detector amplitude and strain. We analyze four seconds of strain data, with a lower cutoff frequency of 20 Hz. Our choice of priors is as detailed in Sec. I of Appendix C in [7].

Figure 20 shows the posterior densities for the $\mathcal{M}-q$ and $q-\chi_{\rm eff}$ subspaces. The consistency between the three waveform models is in agreement with previous studies, demonstrating that systematic errors were below the statistical errors for this event [6,8,123].

2. *NRHybSur3dq8*

In the second example, we inject a NRHybSur3dq8 waveform into a HLV detector network assuming zero-noise and using the Advanced LIGO and Advanced VIRGO design sensitivity PSDs [117,124,125]. The injected waveform was taken to have a mass-ratio of $q=3$, chirp mass of $\mathcal{M}_c=20\,M_\odot$, and spins of $\chi_1=0.6$ and $\chi_2=-0.3$. The luminosity distance was $d_L=1$ Gpc and the sky location, polarization, and coalesence phase were arbitrarily chosen. Priors are again taken to be as detailed in Sec. I of

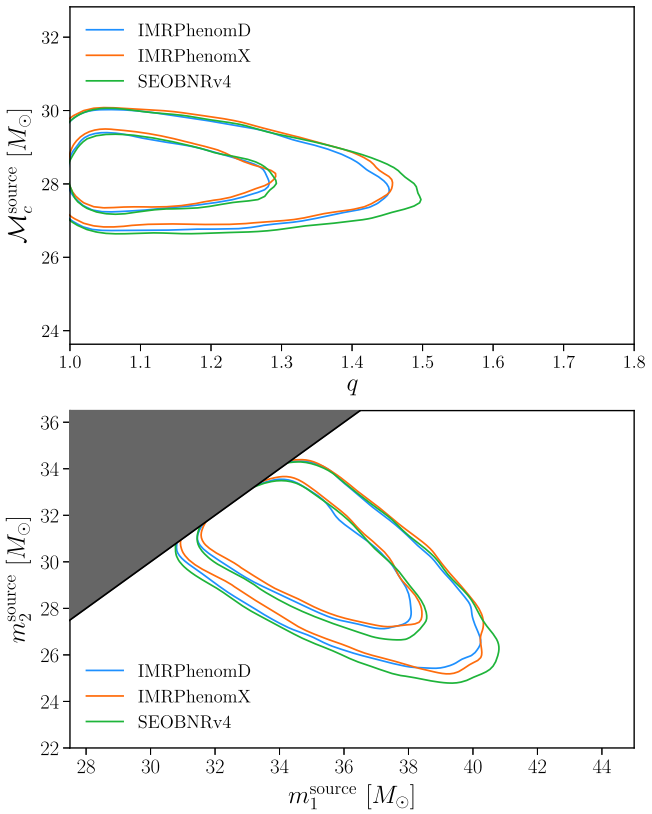

FIG. 20. The top panel shows the $q-\chi_{\rm eff}$ 2D posteriors recovered by IMRPHENOMXAS, IMRPHENOMD, and SEOBNRv4 when analyzing GW150914. All models show excellent agreement. The bottom panel shows the recovered component masses in the source frame using the same waveform models. Note that the black line denotes the equal mass limit and we enforce $m_1>m_2$.

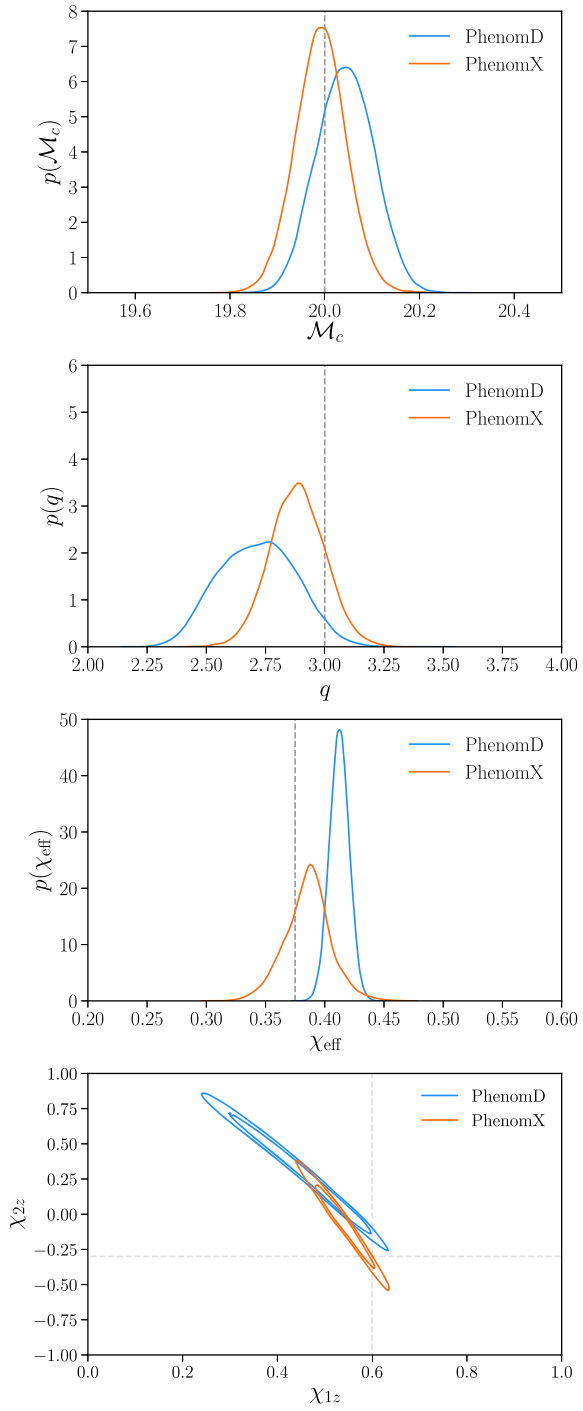

FIG. 21. PE results on an injected NRHybSur3dq8 waveform with parameters $\mathcal{M}_c=20$, $q=3$, $\chi_{1z}=0.6$ and $\chi_{2z}=-0.3$. The first three panels show the 1D posterior distributions for the chirp mass $\mathcal{M}_c$, mass ratio q and effective spin $\chi_{\rm eff}$ as recovered by IMRPHENOMXAS and IMRPHENOMD against an injected NRHybSur3dq8 waveform. The dashed line denotes the injected values. IMRPHENOMXAS demonstrates excellent recovery of the injected parameters with significantly smaller biases and tighter posteriors than those exhibited by IMRPHENOMD. The last panel shows the 2D posterior distributions for χ_{1z} and χ_{2z}, highlighting how improvements in IMRPHENOMXAS enables a more accurate measurement of individual spin components.

Appendix C in [7]. In Fig. 21, we highlight the reduced bias provided by IMRPHENOMXAS over IMRPHENOMD, demonstrating how the advances implemented in IMRPHENOMXAS will help tighten and improve our constraints on the source properties of astrophysical black holes. A detailed study of waveform systematics and parameter biases is beyond the scope of this paper and will be presented in a forthcoming paper.

X. CONCLUSIONS

In this paper we have presented a new model for the dominant $(2, \pm 2)$ spherical harmonics of the gravitational-wave signal from nonprecessing, noneccentric coalescing black holes. In gravitational wave data analysis, this model will most typically be used as part of a multimode waveform, where subdominant modes are included using the IMRPHENOMXHM model, which we present in a companion paper [100]. Furthermore, a technique to accelerate waveform evaluation is available, which drastically reduces computational cost in particular for low masses (or low start frequencies), as discussed in a second companion paper [18]. The model presented here will form the basis for the forthcoming extension to precession and higher modes [20]. Details of how to use the LALsuite [31] implementation of the model are given in Appendix C of [100].

In the following we summarize the main improvements of IMRPHENOMXAS over IMRPHENOMD. Several of the changes affect all of the three frequency regions:

(i) The number of NR waveforms the model is calibrated to has increased from 19 to 652. While IMRPHENOMD was only calibrated to waveforms up to mass ratio 18, IMRPHENOMXAS includes waveforms up to mass ratio 1000, which were computed in the in an appropriate test-particle limit as in [88], see Sec. III.

(ii) IMRPHENOMD modeled 2-dimensional parameter spaces of symmetric mass ratio and effective spin (choosing different effective spins in different frequency regimes as appropriate). IMRPHENOMXAS models the complete 3-dimensional parameter space without effective spin approximations.

(iii) *Ad hoc* parameter space fits have been replaced by a systematic procedure designed to avoid both underfitting and overfitting [25,88], which proceeds by hierarchically treating subspaces like the nonspinning, or equal-spin systems.

(iv) IMRPHENOMXAS incorporates physically motivated transition regions, with the key frequencies obeying a natural hierarchy.

(v) The improvements mentioned above also facilitated a more systematic study regarding the optimal parametrization of a given waveform model, in particular concerning the use of coefficients of basis functions versus the use of collocation points, see Sec. IV A.

(vi) Finally, the implementation in the LAL software library for gravitational wave data analysis [31] has been modularized, to allow independent updates for the inspiral, intermediate and ringdown regions of the phase or amplitude models.

In summary, these improvements lead to a dramatic increase in the accuracy of IMRPHENOMXAS over IMRPHENOMD, as shown in Fig. 18. We find up to 2 orders of magnitude improvement in the mismatches against the SEOBNRv4-NR hybrids across the parameter space and an order of magnitude improvement in the mismatches against the 22-mode for NRHybSur3dq8.

Our description of the inspiral region has improved due to a lower cutoff frequency of 74% of the IMRPHENOMD value for the inspiral calibration, which corresponds to approximately doubling the length of the waveform in the time domain. In addition, the transition frequency from inspiral to the intermediate region is now carefully chosen as a function of parameter space, instead of set to a fixed frequency, as discussed in Sec. V, and different post-Newtonian orders of the underlying TaylorF2 approximant have been compared. Modeling of the intermediate frequency region also greatly benefits from our careful choice of transition frequencies. In addition we have added further degrees of freedom for more accurate fits.

Finally, several changes affect mostly the ringdown, or more generally the highest frequencies:

(i) Hybrid waveforms have been built from the Newman-Penrose scalar ψ_4 (see, e.g., [29]) instead of from the strain, which results in a significantly cleaner ringdown waveform.

(ii) The time resolution for hybrid waveforms has been increased from $M\Delta t = 1$ to $M\Delta t = 0.5$, which benefits high spin cases with high ringdown frequencies.

(iii) The fits for final spin and final mass, which are required for computing the complex ringdown frequency, have been changed from using the 2-dimensional effective spin fits of [16] to modeling the full 3-dimensional parameter space dependency, which eliminates the necessity to model the discrepancy between the value from ringdown frequency according to the fits with an extra parameter.

An important challenge for the future is to improve the modeling of extreme mass ratios, and to study the transition between comparable and extreme mass ratios. An important element here will be to extend the catalogue of accurate and sufficiently long numerical relativity waveforms beyond mass ratio 18.

ACKNOWLEDGMENTS

We thank the internal reviewers of the LIGO and Virgo collaboration for their careful checking of our LALSUITE code implementation and their valuable feedback. We thank Patricia Schmidt for useful discussions and comments on the paper and Nan Jiang for helpful feedback on the

manuscript. We thank the anonymous referee for detailed comments that have really helped to improve this manuscript. We thank Alessandro Nagar, Sebastiano Bernuzzi, and Enno Harms for giving us access to *Teukode* [26–28], which was used to generate our extreme-mass-ratio waveforms. This work was supported by European Union FEDER funds, the Ministry of Science, Innovation and Universities and the Spanish Agencia Estatal de Investigación Grants No. FPA2016-76821-P, No. RED2018-102661-T, No. RED2018-102573-E, No. FPA2017-90687-REDC, Vicepresid'encia i Conselleria d'Innovació, Recerca i Turisme, Conselleria d'Educació, i Universitats del Govern de les Illes Balears i Fons Social Europeu, Generalitat Valenciana (PROMETEO/2019/071), EU COST Actions No. CA18108, No. CA17137, No. CA16214, and No. CA16104, and the Spanish Ministry of Education, Culture and Sport Grants No. FPU15/03344 and No. FPU15/01319. M. C. acknowledges funding from the European Union's Horizon 2020 research and innovation programme, under the Marie Skłodowska-Curie Grant Agreement No. 751492. The authors thankfully acknowledge the computer resources at MareNostrum and the technical support provided by Barcelona Supercomputing Center (BSC) through Grants No. AECT-2019-2-0010, No. AECT-2019-1-0022, No. AECT-2019-2-0017, No. AECT-2019-1-0014, No. AECT-2018-3-0017, No. AECT-2018-2-0022, No. AECT-2018-1-0009, No. AECT-2017-3-0021, No. AECT-2017-3-0013, No. AECT-2017-2-0017, No. AECT-2017-1-0017, No. AECT-2016-3-0014, No. AECT2016-2-0009, from the Red Española de Supercomputación (RES) and PRACE (Grant No. 2015133131). BAM and ET simulations were carried out on the BSC MareNostrum computer under PRACE and RES (Red Española de Supercomputación) allocations and on the FONER computer at the University of the Balearic Islands. Benchmarks calculations were carried out on the cluster CIT provided by LIGO Laboratory and supported by National Science Foundation Grants No. PHY-0757058 and No. PHY-0823459.

APPENDIX A: TAYLORF2

Here we incorporate nonspinning corrections to 3.5PN order, spin-orbit corrections to 3.5PN, spin-orbit tail corrections to 4PN, quadratic-in-spin corrections to 3PN and the cubic-in-spin 3.5PN corrections.

1. Amplitude

The inspiral amplitude is based on the reexpanded PN amplitude TaylorF2

$$A_{\rm PN}(f;\Xi) = A_0 \sum_{i=0}^{6} \mathcal{A}_i (\pi f)^{i/3}, \tag{A1}$$

where $\Xi = \{\eta, \chi_1, \chi_2\}$. The expansion coefficients are given by

$$\mathcal{A}_0 = 1, \tag{A2}$$

$$\mathcal{A}_1 = 0, \tag{A3}$$

$$\mathcal{A}_2 = -\frac{323}{224} + \frac{451\eta}{168}. \tag{A4}$$

$$\mathcal{A}_3 = \chi_1\left(\frac{27\delta}{16} - \frac{11\eta}{12} + \frac{27}{16}\right) + \chi_2\left(-\frac{27\delta}{16} - \frac{11\eta}{12} + \frac{27}{16}\right) \tag{A5}$$

$$\mathcal{A}_4 = {\chi_1}^2\left(-\frac{81\delta}{64} + \frac{81\eta}{32} - \frac{81}{64}\right) + {\chi_2}^2\left(\frac{81\delta}{64} + \frac{81\eta}{32} - \frac{81}{64}\right) + \left(\frac{105271}{24192}\eta^2 - \frac{1975055}{338688}\eta - \frac{27312085}{8128512}\right) - \frac{47}{16}\eta\chi_1\chi_2 \tag{A6}$$

$$\mathcal{A}_5 = {\chi_1}^3\left(\delta\left(\frac{3}{16} - \frac{3\eta}{16}\right) - \frac{9\eta}{16} + \frac{3}{16}\right) + \chi_1\left(\delta\left(\frac{287213}{32256} - \frac{2083\eta}{8064}\right) - \frac{2227\eta^2}{2016} - \frac{15569\eta}{1344} + \frac{287213}{32256}\right) + {\chi_2}^3\left(\delta\left(\frac{3\eta}{16} - \frac{3}{16}\right) - \frac{9\eta}{16} + \frac{3}{16}\right) + \chi_2\left(\delta\left(\frac{2083\eta}{8064} - \frac{287213}{32256}\right) - \frac{2227\eta^2}{2016} - \frac{15569\eta}{1344} + \frac{287213}{32256}\right) - \frac{85\pi}{64} + \frac{85\pi\eta}{16} \tag{A7}$$

$$\mathcal{A}_6 = \chi_1\left(-\frac{17\pi\delta}{12} + \left(-\frac{133249\eta^2}{8064} - \frac{319321\eta}{32256}\right)\chi_2 + \frac{5\pi\eta}{3} - \frac{17\pi}{12}\right) + {\chi_1}^2\left(\delta\left(-\frac{141359\eta}{32256} - \frac{49039}{14336}\right) + \frac{163199\eta^2}{16128} + \frac{158633\eta}{64512} - \frac{49039}{14336}\right) + {\chi_2}^2\left(\delta\left(\frac{141359\eta}{32256} + \frac{49039}{14336}\right) + \frac{163199\eta^2}{16128} + \frac{158633\eta}{64512} - \frac{49039}{14336}\right) + \chi_2\left(\frac{17\pi\delta}{12} + \frac{5\pi\eta}{3} - \frac{17\pi}{12}\right) - \frac{177520268561}{8583708672} + \left(\frac{545384828789}{5007163392} - \frac{205\pi^2}{48}\right)\eta - \frac{3248849057\eta^2}{178827264} + \frac{34473079\eta^3}{6386688} \tag{A8}$$

2. Phase

The underlying frequency-domain phasing model in IMRPhenomX is based on the TaylorF2 post-Newtonian approximant constructed via the application of the stationary phase approximation (SPA). For quasicircular, nonprecessing binaries, the input ingredients are the center-of-mass energy E and the energy flux F. The canonical TaylorF2 approximant used in IMRPhenomX implements recent tail-induced spin-orbit terms at 4PN, cubic-in-spin corrections at 3.5PN and quadratic-in-spin corrections at 3PN. Schematically, the energy can be written as

$$E = -\frac{\eta}{2} x [E_{\rm NS} + x^{3/2} E_{\rm SO} + x^2 E_{\rm SS} + x^{7/2} E_{\rm SSS}] \quad \text{(A9)}$$

where $E_{\rm NS}$, $E_{\rm SO}$, $E_{\rm SS}$ and $E_{\rm SSS}$ the nonspinning, spin-orbit, quadratic-in-spin and cubic-in-spin corrections to the energy. Although the nonspinning contributions are currently known to 4PN, the baseline model presented here restricts the nonspinning contributions to 3PN. The spin-orbit terms begin at 1.5PN order are currently known to 3.5PN [106,107]. The quadratic-in-spin corrections are known at next-to-leading order, coresponding to 3PN [107]. The cubic-in-spin terms are currently known to leading order and enter the energy and flux at 3.5PN [106].

Similarly, the flux can be written as

$$\mathcal{F} = \frac{32}{5} \eta x^5 [\mathcal{F}_{\rm NS} + x^{3/2} \mathcal{F}_{\rm SO} + x^2 \mathcal{F}_{\rm SS} + x^{7/2} \mathcal{F}_{\rm SSS}] \quad \text{(A10)}$$

where $\mathcal{F}_{\rm NS}$, $\mathcal{F}_{\rm SO}$, $\mathcal{F}_{\rm SS}$ and $\mathcal{F}_{\rm SSS}$ denote the nonspinning, spin-orbit, quadratic-in-spin and cubic-in-spin corrections to post-Newtonian energy flux.

The frequency-domain phase from the TaylorF2 terms is given by

$$\varphi_{\rm TF2}(f;\Xi) = 2\pi f t_c - \varphi_c - \frac{\pi}{4} + \frac{3}{128\eta} (\pi f M)^{-5/3} \sum_{i=0}^{7} \varphi_i(\Xi) (\pi f M)^{i/3}. \quad \text{(A11)}$$

In IMRPHENOMD, the TaylorF2 baseline was based on nonspinning corrections to 3.5PN, linear spin-orbit corrections to 3.5PN and quadratic spin corrections to 2PN. In addition, upon re-expanding the PN energy and flux in deriving the TaylorF2 phase, all quadratic and higher spin corrections beyond 2PN were implicitly dropped. The coefficients used in IMRPHENOMXAS incorporate relative 1PN quadratic-in-spin corrections, the leading-order cubic-in-spin corrections and a tail-induced SO term entering at 4PN, φ_8. The coefficients detailed below define the *canonical* TaylorF2 model discussed in Sec. VII A

$$\varphi_0 = 1 \quad \text{(A12)}$$

$$\varphi_1 = 0 \quad \text{(A13)}$$

$$\varphi_2 = \frac{55\eta}{9} + \frac{3715}{756} \quad \text{(A14)}$$

$$\varphi_3 = \frac{113\delta\chi_a}{3} + \left(\frac{113}{3} - \frac{76\eta}{3}\right)\chi_s - 16\pi \quad \text{(A15)}$$

$$\varphi_4 = -\frac{405}{4}\delta\chi_a\chi_s + \left(200\eta - \frac{405}{8}\right)\chi_a^2 + \left(\frac{5\eta}{2} - \frac{405}{8}\right)\chi_s^2 + \frac{15293365}{508032} + \frac{27145}{504}\eta + \frac{3085}{72}\eta^2 \quad \text{(A16)}$$

$$\begin{aligned}\varphi_5 = {} & \chi_a\left(-\frac{140\delta\eta}{9} - \frac{732985\delta}{2268} + \left(-\frac{140\delta\eta}{9} - \frac{732985\delta}{2268}\right)\log(\pi f)\right) \\ & + \chi_s\left(\left(\frac{340\eta^2}{9} + \frac{24260\eta}{81} - \frac{732985}{2268}\right)\log(\pi f) + \frac{340\eta^2}{9} + \frac{24260\eta}{81} - \frac{732985}{2268}\right) \\ & + \left(\frac{38645\pi}{756} - \frac{65\pi\eta}{9}\right)\log(\pi f) - \frac{65\pi}{9}\eta + \frac{38645\pi}{756}\end{aligned} \quad \text{(A17)}$$

$$\begin{aligned}\varphi_6 = {} & \chi_s\left(\chi_a\left(\frac{75515\delta}{144} - \frac{8225\delta\eta}{18}\right) - 520\pi\eta + \frac{2270\pi}{3}\right) + \frac{2270\pi\delta\chi_a}{3} - \frac{6848}{63}\log(\pi f) - \frac{127825\eta^3}{1296} \\ & + \left(-480\eta^2 - \frac{263245\eta}{252} + \frac{75515}{288}\right)\chi_a^2 + \left(\frac{1255\eta^2}{9} - \frac{232415\eta}{504} + \frac{75515}{288}\right)\chi_s^2 \\ & + \frac{76055\eta^2}{1728} + \frac{2255\pi^2\eta}{12} - \frac{15737765635\eta}{3048192} - \frac{640\pi^2}{3} - \frac{6848\gamma_E}{21} + \frac{11583231236531}{4694215680} - \frac{13696\log(2)}{21}\end{aligned} \quad \text{(A18)}$$

$$\varphi_7 = \chi_a\left(-\frac{1985\delta\eta^2}{48}+\frac{26804935\delta\eta}{6048}-\frac{251500837750\delta}{3048192}\right)$$
$$+\chi_s\left(-1140\pi\delta\chi_a+\frac{5345\eta^3}{36}+\left(80\eta^2-7270\eta+\frac{14585}{8}\right)\chi_a^2-\frac{1042165\eta^2}{3024}+\frac{10566655595\eta}{762048}-\frac{25150083775}{3048192}\right)$$
$$+\chi_a^3\left(\frac{14585\delta}{24}-2380\delta\eta\right)+\chi_s^2\left(\chi a\left(\frac{14585\delta}{8}-\frac{215\delta\eta}{2}\right)+40\pi\eta-570\pi\right)+\left(\frac{100\eta^2}{3}-\frac{475\eta}{6}+\frac{14585}{24}\right)\chi_s^3$$
$$-\frac{74045\pi\eta^2}{756}+(2240\pi\eta-570\pi)\chi_a^2+\frac{378515\pi\eta}{1512}+\frac{77096675\pi}{254016} \tag{A19}$$

$$\varphi_8 = \pi\left[\chi_a\left(-\frac{99185}{252}\delta\eta+\frac{233915\delta}{168}+\left(\frac{99185\delta\eta}{252}-\frac{233915\delta}{168}\right)\log(\pi f)\right)\right.$$
$$\left.+\chi_s\left(\left(-\frac{19655\eta^2}{189}+\frac{3970375\eta}{2268}-\frac{233915}{168}\right)\log(\pi f)+\frac{19655\eta^2}{189}-\frac{3970375\eta}{2268}+\frac{233915}{168}\right)\right]. \tag{A20}$$

3. Extending results to 4.5PN

An implicit and powerful feature of the current generation of phenomenological waveform models is the implicit modularity. By separating the waveform into three key regimes we are free to recalibrate or improve aspects of the waveform model in reaction to the latest developments in the literature. A worked example of this would be the extension of the results to include the latest 4PN and 4.5PN results in the literature. For the nonspinning sector, the equations of motion for compact binaries has been derived to 4PN [108,109,111,113,126] leading to an additional nonspinning term of the form

$$E^{\rm 4PN} = x^4\left[\frac{77}{31104}\eta^4+\frac{301}{1728}\eta^3+\left(\frac{3157\pi^2}{576}-\frac{498449}{3456}\right)\eta^2+\eta\left(\frac{448}{15}\log(16x)+\frac{9037\pi^2}{1536}+\frac{896}{15}\gamma_E-\frac{123671}{5760}\right)-\frac{3969}{128}\right]. \tag{A21}$$

As well as the 4PN derivation above, higher nonlinear tail effects associated to quartic nonlinear interactions have recently been derived from first principles in the MPM formalism [114] as well as an independent derivation from the PN reexpansion of the factorized and resummed EOB fluxes [95]. Such interactions lead to a 4.5PN contribution to the flux

$$\mathcal{F}^{\rm 4.5PN}_{\rm Tail} = \pi x^{9/2}\left[-\frac{3719141\eta^3}{38016}-\frac{133112905\eta^2}{290304}+\left(\frac{2062241}{22176}+\frac{41\pi^2}{12}\right)\eta-\frac{3424}{105}\log(16x)-\frac{6848\gamma}{105}+\frac{265978667519}{745113600}\right]. \tag{A22}$$

Another interesting contribution derived from the PN re-expansion of the EOB fluxes is the identification of a leading-order tail-induced spin-spin term in the flux [95][3]

$$\mathcal{F}^{\rm 3.5PN}_{\rm LO\text{-}SS,Tail} = \pi x^{7/2}\left[\left(8\delta^2+\frac{1}{8}\right)\chi_a^2+\left(\frac{\delta^2}{8}+8\right)\chi_s^2+\frac{65}{4}\delta\chi_a\chi_s\right], \tag{A23}$$

which coincides with the known test-particle limit [127]. Adding these terms to the PN flux and energy, we find the following higher order contributions to the PN phasing

$$\varphi_7^N = -\pi x^{7/2}\left[-325\delta\chi_a\chi_s+\left(640\eta-\frac{325}{2}\right)\chi_a^2+\left(10\eta-\frac{325}{2}\right)\chi_s^2\right] \tag{A24}$$

$$\varphi_9^N = \pi x^{9/2}\left[\frac{10323755}{199584}\eta^3+\frac{45293335}{127008}\eta^2+\left(-\frac{1492917260735}{134120448}+\frac{2255\pi^2}{6}\right)\eta\right.$$
$$\left.-\frac{6848\log(x)}{21}-\frac{640\pi^2}{3}-\frac{13696}{21}\gamma_E+\frac{105344279473163}{18776862720}-\frac{27392\log(2)}{21}\right], \tag{A25}$$

[3]Using an appropriate change in spin variables from the notation of [95].

in agreement with [95,128]. A somewhat more vexing task is how to incorporate, in a fully consistent way, the incomplete knowledge at 4PN. One possible approach, as taken in [95], is to construct an approximant that depends on as of yet unknown analytical coefficients c_N, allowing the incomplete 4 and 4.5PN terms to be included in a fully consistent way, complete with η dependence. Here, however, we choose to drop the unknown analytical information and instead absorb these into the pseudo-PN calibration. In practice, we do not find any significant difference between the canonical TaylorF2 approximant used and the higher order PN expressions given here after the pseudo-PN calibration is taken into account. The *extended* TaylorF2 approximant discussed in Sec. VII A uses the coefficients detailed in Eqs. (A12) to (A21) plus the additional terms in Eqs. (A24) and (A25).

APPENDIX B: STATIONARY PHASE APPROXIMATION

Here we overview the stationary phase approximation (SPA) applied to a time domain signal [32,33,129]

$$h_{\ell m}(t) = A_{\ell m}(t) e^{-im\varphi(t)}.$$

The orbital phase φ is related to the orbital frequency by $\omega = \dot{\varphi}$. The SPA approximation is formally valid if the following criteria are met [32,33,130]

$$\left|\frac{\dot{A}/A}{\omega}\right| \ll 1, \qquad \left|\frac{\dot{\omega}}{\omega^2}\right| \ll 1, \qquad \left|\frac{(\dot{A}/A)^2}{\dot{\omega}}\right| \ll 1.$$

The SPA approximation works as the Fourier transform of a signal is highly oscillatory and unless there are strong cancellations between the orbital phase $\varphi(t)$ and the $2\pi ft$ term, the Fourier transform will have support that is roughly centered on the point of stationary phase. This enables us to define a time as a function of the frequency

$$m\omega(t_f) = 2\pi f,$$

where t_f is strictly only valid in the SPA regime. Assuming a monotonically increasing orbital phase, such that $\omega > 0$ and $\dot{\omega} > 0$, then we can expand the signal about the SPA time

$$\tilde{h}_{\rm SPA}(f) \simeq A_{\ell m}(t_f) e^{2\pi i f t_f - mi\varphi(t_f)} \int e^{-i(t-t_f)^2 m\dot{\omega}(t_f)/2} dt$$

Noting that $|(\dot{A}/A)^2/\dot{\omega}| \ll 1$, we can treat the amplitude as being approximately constant. Performing the Gaussian integration, we find

$$\begin{aligned}
\tilde{h}_{\ell m}(f) &\simeq A_{\ell m}(f) e^{-i\Psi_{\ell m}(f)}, \\
A_{\ell m}(f) &\simeq A_{\ell m}(t_f)\sqrt{\frac{2\pi}{m\dot{\omega}(t_f)}}, \\
\Psi_{\ell m}(f) &\simeq m\varphi(t_f) - 2\pi f t_f + \frac{\pi}{4},
\end{aligned}$$

where we have made use of the standard integral $\int_{-\infty}^{\infty} dx e^{-ix^2} = \sqrt{\pi} e^{-i\pi/4}$. This can now be expressed in terms of the TaylorF2 phase $\varphi^{\rm TF2}_{\ell m}$ and a phase shift $\varphi_{0,\ell m}$

$$\Psi_{\ell m}(f) \simeq -2\pi f t_0 + \frac{\pi}{4} + \varphi_{0,\ell m} + \varphi^{\rm TF2}_{\ell m}(f)$$

where

$$\varphi_{0,\ell m} = \frac{m}{2}\varphi_{0,22} + \varphi^{\rm Amp}_{\ell m},$$

and

$$\varphi^{\rm TF2}_{\ell m}(f) = \frac{m}{2}\varphi^{\rm TF2}_{22}\left(\frac{2f}{m}\right). \tag{B1}$$

The term $\varphi^{\rm Amp}_{\ell m}$ corresponds to phase corrections arising from the complex PN amplitudes and $\varphi_{0,\ell,m}$ a gauge freedom associated to phase shifts. Collecting this all together, we can write the SPA of the time domain mode as

$$\tilde{h}_{\ell m}(f) = A_{\ell m}(t_f)\sqrt{\frac{2\pi}{m\dot{\omega}}} e^{i[2\pi f t_f - m\varphi(t_f) - \pi/4]}. \tag{B2}$$

[1] S. A. Usman *et al.*, Classical Quantum Gravity **33**, 215004 (2016).
[2] S. Sachdev *et al.*, arXiv:1901.08580.
[3] J. Veitch *et al.*, Phys. Rev. D **91**, 042003 (2015).
[4] G. Ashton *et al.*, Astrophys. J. Suppl. Ser. **241**, 27 (2019).
[5] B. P. Abbott *et al.* (LIGO Scientific and Virgo Collaborations), Phys. Rev. Lett. **116**, 061102 (2016).
[6] B. P. Abbott *et al.* (LIGO Scientific and Virgo Collaborations), Phys. Rev. Lett. **116**, 241102 (2016).
[7] B. P. Abbott *et al.* (LIGO Scientific and Virgo Collaborations), Phys. Rev. X **9**, 031040 (2019).
[8] B. P. Abbott *et al.* (LIGO Scientific and Virgo Collaborations), Classical Quantum Gravity **34**, 104002 (2017).

[9] Y. Pan, A. Buonanno, A. Taracchini, L. E. Kidder, A. H. Mroué, H. P. Pfeiffer, M. A. Scheel, and B. Szilágyi, Phys. Rev. D **89**, 084006 (2014).
[10] A. Taracchini *et al.*, Phys. Rev. D **89**, 061502 (2014).
[11] M. Pürrer, Phys. Rev. D **93**, 064041 (2016).
[12] A. Bohé *et al.*, Phys. Rev. D **95**, 044028 (2017).
[13] S. Babak, A. Taracchini, and A. Buonanno, Phys. Rev. D **95**, 024010 (2017).
[14] M. Hannam, P. Schmidt, A. Bohé, L. Haegel, S. Husa, F. Ohme, G. Pratten, and M. Pürrer, Phys. Rev. Lett. **113**, 151101 (2014).
[15] S. Husa, S. Khan, M. Hannam, M. Pürrer, F. Ohme, X. Jiménez Forteza, and A. Bohé, Phys. Rev. D **93**, 044006 (2016).
[16] S. Khan, S. Husa, M. Hannam, F. Ohme, M. Pürrer, X. Jiménez Forteza, and A. Bohé, Phys. Rev. D **93**, 044007 (2016).
[17] L. London, S. Khan, E. Fauchon-Jones, C. García, M. Hannam, S. Husa, X. Jiménez-Forteza, C. Kalaghatgi, F. Ohme, and F. Pannarale, Phys. Rev. Lett. **120**, 161102 (2018).
[18] C. García-Quirós, S. Husa, M. Mateu-Lucena, and A. Borchers, arXiv:2001.10897.
[19] S. Vinciguerra, J. Veitch, and I. Mandel, Classical Quantum Gravity **34**, 115006 (2017).
[20] G. Pratten, C. García Quirós, M. Colleoni, A. Ramos-Buades, H. Estellés, M. Mateu, R. Jaume, and S. Husa, arXiv:2004.06503.
[21] S. Khan, K. Chatziioannou, M. Hannam, and F. Ohme, Phys. Rev. D **100**, 024059 (2019).
[22] P. Ajith *et al.*, Phys. Rev. Lett. **106**, 241101 (2011).
[23] L. Santamaria *et al.*, Phys. Rev. D **82**, 064016 (2010).
[24] P. Kumar, T. Chu, H. Fong, H. P. Pfeiffer, M. Boyle, D. A. Hemberger, L. E. Kidder, M. A. Scheel, and B. Szilagyi, Phys. Rev. D **93**, 104050 (2016).
[25] X. Jiménez-Forteza, D. Keitel, S. Husa, M. Hannam, S. Khan, and M. Pürrer, Phys. Rev. D **95**, 064024 (2017).
[26] E. Harms, S. Bernuzzi, A. Nagar, and A. Zenginoglu, Classical Quantum Gravity **31**, 245004 (2014).
[27] E. Harms, G. Lukes-Gerakopoulos, S. Bernuzzi, and A. Nagar, Phys. Rev. D **93**, 044015 (2016); **100**, 129901(A) (2019).
[28] E. Harms, G. Lukes-Gerakopoulos, S. Bernuzzi, and A. Nagar, Phys. Rev. D **94**, 104010 (2016).
[29] S. Husa, M. Colleoni, H. Estellés, G. Q. Cecilio, A. Ramos-Buades, G. Pratten, R. Jaume, X. Jimenez-Forteza, and D. Keitel (to be published).
[30] Y. Wiaux, L. Jacques, and P. Vandergheynst, J. Comput. Phys. **226**, 2359 (2007).
[31] The LIGO Scientific Collaboration, LALSuite: LSC Algorithm Library Suite, https://www.lsc-group.phys.uwm.edu/daswg/projects/lalsuite.html (2015).
[32] L. S. Finn and D. F. Chernoff, Phys. Rev. D **47**, 2198 (1993).
[33] C. Cutler and E. E. Flanagan, Phys. Rev. D **49**, 2658 (1994).
[34] T. Damour, B. R. Iyer, and B. S. Sathyaprakash, Phys. Rev. D **62**, 084036 (2000).
[35] J. Calderón Bustillo, A. Bohé, S. Husa, A. M. Sintes, M. Hannam, and M. Pürrer, arXiv:1501.00918.
[36] L. Blanchet, Living Rev. Relativity **17**, 2 (2014).
[37] T. Damour, Phys. Rev. D **64**, 124013 (2001).
[38] T. Damour, B. R. Iyer, and B. S. Sathyaprakash, Phys. Rev. D **66**, 027502 (2002).
[39] K. G. Arun, B. R. Iyer, B. S. Sathyaprakash, and P. A. Sundararajan, Phys. Rev. D **71**, 084008 (2005); **72**, 069903 (E) (2005).
[40] A. Buonanno, B. Iyer, E. Ochsner, Y. Pan, and B. S. Sathyaprakash, Phys. Rev. D **80**, 084043 (2009).
[41] K. Kokkotas and B. Schmidt, Living Rev. Relativity **2**, 2 (1999).
[42] M. Cabero, A. B. Nielsen, A. P. Lundgren, and C. D. Capano, Phys. Rev. D **95**, 064016 (2017).
[43] L. N. Trefethen, *Finite Difference and Spectral Methods for Ordinary and Partial Differential Equations* (1996), http://people.maths.ox.ac.uk/trefethen/pdetext.html.
[44] M. Luna and A. M. Sintes, Classical Quantum Gravity **23**, 3763 (2006).
[45] A. Kumar Mehta, P. Tiwari, N. K. Johnson-McDaniel, C. K. Mishra, V. Varma, and P. Ajith, Phys. Rev. D **100**, 024032 (2019).
[46] P. Ajith *et al.*, Classical Quantum Gravity **24**, S689 (2007).
[47] P. Ajith *et al.*, Phys. Rev. D **77**, 104017 (2008); **79**, 129901 (E) (2009).
[48] S. T. McWilliams, Phys. Rev. Lett. **122**, 191102 (2019).
[49] A. Buonanno and T. Damour, Phys. Rev. D **59**, 084006 (1999).
[50] A. Buonanno and T. Damour, Phys. Rev. D **59**, 084006 (1999).
[51] A. Nagar *et al.*, Phys. Rev. D **98**, 104052 (2018).
[52] S. Ossokine, L. E. Kidder, and H. P. Pfeiffer, Phys. Rev. D **88**, 084031 (2013).
[53] D. A. Hemberger, M. A. Scheel, L. E. Kidder, B. Szilagyi, G. Lovelace, N. W Taylor, and S. A Teukolsky, Classical Quantum Gravity **30**, 115001 (2013).
[54] B. Szilagyi, L. Lindblom, and M. A. Scheel, Phys. Rev. D **80**, 124010 (2009).
[55] M. A. Scheel, M. Boyle, T. Chu, L. E. Kidder, K. D. Matthews, and H. P. Pfeiffer, Phys. Rev. D **79**, 024003 (2009).
[56] M. Boyle, D. A. Brown, L. E. Kidder, A. H. Mroué, H. P. Pfeiffer, M. A. Scheel, G. B. Cook, and S. A. Teukolsky, Phys. Rev. D **76**, 124038 (2007).
[57] A. H. Mroué, M. A. Scheel, B. Szilagyi, H. P. Pfeiffer, M. Boyle *et al.*, Phys. Rev. Lett. **111**, 241104 (2013).
[58] L. T. Buchman, H. P. Pfeiffer, M. A. Scheel, and B. Szilagyi, Phys. Rev. D **86**, 084033 (2012).
[59] B. Bruegmann, J. A. Gonzalez, M. Hannam, S. Husa, U. Sperhake, and W. Tichy, Phys. Rev. D **77**, 024027 (2008).
[60] S. Husa, J. A. Gonzalez, M. Hannam, B. Bruegmann, and U. Sperhake, Classical Quantum Gravity **25**, 105006 (2008).
[61] M. Babiuc-Hamilton *et al.*, The Einstein toolkit, 2019, to find out more, visit http://einsteintoolkit.org.
[62] M. Campanelli, C. O. Lousto, P. Marronetti, and Y. Zlochower, Phys. Rev. Lett. **96**, 111101 (2006).
[63] T. Nakamura, K. Oohara, and Y. Kojima, Prog. Theor. Phys. Suppl. **90**, 1 (1987).
[64] M. Shibata and T. Nakamura, Phys. Rev. D **52**, 5428 (1995).

[65] T. W. Baumgarte and S. L. Shapiro, Phys. Rev. D **59**, 024007 (1999).
[66] S. Brandt and B. Brügmann, Phys. Rev. Lett. **78**, 3606 (1997).
[67] J. M. Bowen, J. York, and W. James, Phys. Rev. D **21**, 2047 (1980).
[68] M. Ansorg, B. Brügmann, and W. Tichy, Phys. Rev. D **70**, 064011 (2004).
[69] P. Marronetti, W. Tichy, B. Bruegmann, J. Gonzalez, and U. Sperhake, Phys. Rev. D **77**, 064010 (2008).
[70] J. D. Brown, P. Diener, O. Sarbach, E. Schnetter, and M. Tiglio, Phys. Rev. D **79**, 044023 (2009).
[71] J. G. Baker, J. Centrella, D.-I. Choi, M. Koppitz, and J. van Meter, Phys. Rev. Lett. **96**, 111102 (2006).
[72] C. Bona, J. Masso, E. Seidel, and J. Stela, Phys. Rev. Lett. **75**, 600 (1995).
[73] M. Alcubierre, B. Brügmann, P. Diener, M. Koppitz, D. Pollney, E. Seidel, and R. Takahashi, Phys. Rev. D **67**, 084023 (2003).
[74] B. Gustaffsson, H. O. Kreiss, and J. Oliger, *Time Dependent Problems and Difference Methods* (Wiley, New York, 1995).
[75] E. Schnetter, S. H. Hawley, and I. Hawke, Classical Quantum Gravity **21**, 1465 (2004).
[76] E. Schnetter, P. Diener, E. N. Dorband, and M. Tiglio, Classical Quantum Gravity **23**, S553 (2006).
[77] D. Pollney, C. Reisswig, E. Schnetter, N. Dorband, and P. Diener, Phys. Rev. D **83**, 044045 (2011).
[78] A. Ramos-Buades, S. Husa, and G. Pratten, Phys. Rev. D **99**, 023003 (2019).
[79] L. Lindblom, M. A. Scheel, L. E. Kidder, R. Owen, and O. Rinne, Classical Quantum Gravity **23**, S447 (2006).
[80] H. Friedrich, Commun. Math. Phys. **100**, 525 (1985).
[81] F. Pretorius, Classical Quantum Gravity **22**, 425 (2005).
[82] D. Garfinkle, Phys. Rev. D **65**, 044029 (2002).
[83] J. W. York, Jr., Phys. Rev. Lett. **82**, 1350 (1999).
[84] H. P. Pfeiffer and J. W. York, Jr., Phys. Rev. D **67**, 044022 (2003).
[85] H. P. Pfeiffer, L. E. Kidder, M. A. Scheel, and S. A. Teukolsky, Comput. Phys. Commun. **152**, 253 (2003).
[86] G. Lovelace, R. Owen, H. P. Pfeiffer, and T. Chu, Phys. Rev. D **78**, 084017 (2008).
[87] M. Boyle *et al.*, Classical Quantum Gravity **36**, 195006 (2019).
[88] D. Keitel *et al.*, Phys. Rev. D **96**, 024006 (2017).
[89] A. Nagar, T. Damour, and A. Tartaglia, Classical Quantum Gravity **24**, S109 (2007).
[90] T. Damour and A. Nagar, Phys. Rev. D **76**, 064028 (2007).
[91] T. Damour, B. R. Iyer, and A. Nagar, Phys. Rev. D **79**, 064004 (2009).
[92] S. Bernuzzi, A. Nagar, and A. Zenginoglu, Phys. Rev. D **83**, 064010 (2011).
[93] S. Bernuzzi, A. Nagar, and A. Zenginoglu, Phys. Rev. D **84**, 084026 (2011).
[94] A. Nagar and A. Shah, Phys. Rev. D **94**, 104017 (2016).
[95] F. Messina, A. Maldarella, and A. Nagar, Phys. Rev. D **97**, 084016 (2018).
[96] A. Nagar, F. Messina, C. Kavanagh, G. Lukes-Gerakopoulos, N. Warburton, S. Bernuzzi, and E. Harms, Phys. Rev. D **100**, 104056 (2019).
[97] A. Nagar, G. Pratten, G. Riemenschneider, and R. Gamba, Phys. Rev. D **101**, 024041 (2020).
[98] A. Nagar, G. Riemenschneider, G. Pratten, P. Rettegno, and F. Messina, Phys. Rev. D **102**, 024077 (2020).
[99] K. Weierstrass, in *Sitzungsberichte der Königlich Preußischen Akademie der Wissenschaften zu Berlin* (Erste Mitteilung, Berlin-Brandenburgische Akademie der Wissenschaften, 1885), p. 633.
[100] C. García-Quirós, M. Colleoni, S. Husa, H. Estellés, G. Pratten, A. Ramos-Buades, M. Mateu-Lucena, and R. Jaume, following paper, Phys. Rev. D **102**, 064002 (2020).
[101] E. Racine, Phys. Rev. D **78**, 044021 (2008).
[102] E. Poisson and C. M. Will, Phys. Rev. D **52**, 848 (1995).
[103] P. Ajith, Phys. Rev. D **84**, 084037 (2011).
[104] M. Pürrer, M. Hannam, P. Ajith, and S. Husa, Phys. Rev. D **88**, 064007 (2013).
[105] S. Ossokine, T. Dietrich, E. Foley, R. Katebi, and G. Lovelace, Phys. Rev. D **98**, 104057 (2018).
[106] S. Marsat, Classical Quantum Gravity **32**, 085008 (2015).
[107] A. Bohé, G. Faye, S. Marsat, and E. K. Porter, Classical Quantum Gravity **32**, 195010 (2015).
[108] T. Damour, P. Jaranowski, and G. Schäfer, Phys. Rev. D **89**, 064058 (2014).
[109] L. Bernard, L. Blanchet, A. Bohé, G. Faye, and S. Marsat, Phys. Rev. D **93**, 084037 (2016).
[110] L. Bernard, L. Blanchet, A. Bohé, G. Faye, and S. Marsat, Phys. Rev. D **95**, 044026 (2017).
[111] T. Damour and P. Jaranowski, Phys. Rev. D **95**, 084005 (2017).
[112] L. Bernard, L. Blanchet, A. Bohé, G. Faye, and S. Marsat, Phys. Rev. D **96**, 104043 (2017).
[113] T. Marchand, L. Bernard, L. Blanchet, and G. Faye, Phys. Rev. D **97**, 044023 (2018).
[114] T. Marchand, L. Blanchet, and G. Faye, Classical Quantum Gravity **33**, 244003 (2016).
[115] E. Berti, V. Cardoso, and A. O. Starinets, Classical Quantum Gravity **26**, 163001 (2009).
[116] See Supplemental Material at http://link.aps.org/supplemental/10.1103/PhysRevD.102.064001, for phenomenological fits.
[117] J. Aasi *et al.* (LIGO Scientific Collaboration), Classical Quantum Gravity **32**, 115012 (2015).
[118] D. Shoemaker, https://dcc.ligo.org/cgi-bin/DocDB/ShowDocument?docid=2974.
[119] V. Varma, S. E. Field, M. A. Scheel, J. Blackman, L. E. Kidder, and H. P. Pfeiffer, Phys. Rev. D **99**, 064045 (2019).
[120] LIGO Scientific and Virgo Collaborations, Gravitational wave open science center, https://www.gw-openscience.org (2019).
[121] LIGO Scientific and Virgo Collaborations, Calibration uncertainty envelope release for gwtc-1, https://dcc.ligo.org/LIGO-P1900040/public (2018).
[122] LIGO Scientific and Virgo Collaborations, Power spectral densities (psd) release for gwtc-1, https://dcc.ligo.org/LIGO-P1900011/public (2018).
[123] T. D. Abbott *et al.* (LIGO Scientific and Virgo Collaborations), Phys. Rev. X **6**, 041014 (2016).

[124] L. Barsotti, P. Fritschel, M. Evans, and S. Gras, The updated advanced ligo design curve, https://dcc.ligo.org/LIGO-T1800044 (2018).
[125] F. Acernese *et al.* (VIRGO Collaboration), Classical Quantum Gravity **32**, 024001 (2015).
[126] P. Jaranowski and G. Schäfer, Phys. Rev. D **92**, 124043 (2015).
[127] H. Tagoshi, M. Shibata, T. Tanaka, and M. Sasaki, Phys. Rev. D **54**, 1439 (1996).
[128] A. Nagar, F. Messina, P. Rettegno, D. Bini, T. Damour, A. Geralico, S. Akcay, and S. Bernuzzi, Phys. Rev. D **99**, 044007 (2019).
[129] S. Droz, D. J. Knapp, E. Poisson, and B. J. Owen, Phys. Rev. D **59**, 124016 (1999).
[130] S. Marsat and J. G. Baker, arXiv:1806.10734.